Element release and reaction-induced porosity alteration during shale-hydraulic fracturing fluid interactions

Anna L. Harrison[a,b*,1], Adam D. Jew[a,b], Megan K. Dustin[a], Dana L. Thomas[a],
Claresta M. Joe-Wong[a], John R. Bargar[b], Natalie Johnson[c], Gordon E. Brown Jr.[a,b,c] , and
Katharine Maher[a]

[a]Department of Geological Sciences, 450 Serra Mall, Stanford University, Stanford, CA
94305, USA.

[b]Stanford Synchrotron Radiation Lightsource, SLAC National Accelerator Laboratory,
2575 Sand Hill Road, Menlo Park, CA, 94025, USA.

[c]Department of Photon Science, SLAC National Accelerator Laboratory, 2575 Sand Hill
Road, Menlo Park, CA, 94025, USA

[1]Present address: Department of Earth Sciences, University College London, Gower
Street, London, WC1E 6BT, UK. *ALH - anna.harrison@ucl.ac.uk

*Corresponding author (phone: 1 650 723-2544; facsimile: 1 650 725-2199; e-mail: anna.harrison@ucl.ac.uk).

Abstract

The use of hydraulic fracturing techniques to extract oil and gas from low permeability shale reservoirs has increased significantly in recent years. During hydraulic fracturing, large volumes of water, often acidic and oxic, are injected into shale formations. This drives fluid-rock interaction that can release metal contaminants (*e.g.*, U, Pb) and alter the permeability of the rock, impacting the transport and recovery of water, hydrocarbons, and contaminants. To identify the key geochemical processes that occur upon exposure of shales to hydraulic fracturing fluid, we investigated the chemical interaction of hydraulic fracturing fluids with a variety of shales of different mineralogical texture and composition. Batch reactor experiments revealed that the dissolution of both pyrite and carbonate minerals occurred rapidly, releasing metal contaminants and generating porosity. Oxidation of pyrite and aqueous Fe drove precipitation of Fe(III)-(oxy)hydroxides that attenuated the release of these contaminants via co-precipitation and/or adsorption. The precipitation of these (oxy)hydroxides appeared to limit the extent of pyrite reaction. Enhanced removal of metals and contaminants in reactors with higher fluid pH was inferred to reflect increased Fe-(oxy)hydroxide precipitation associated with more rapid aqueous Fe(II) oxidation. The precipitation of both Al- and Fe-bearing phases revealed the potential for the occlusion of pores and fracture apertures, whereas the selective dissolution of calcite generated porosity. These pore-scale alterations of shale texture and the cycling of contaminants indicate that chemical interactions between shales and hydraulic fracturing fluids may exert an important control on the efficiency of hydraulic fracturing operations and the quality of water recovered at the surface.

1. Introduction

The extraction of oil and gas resources from low permeability shale reservoirs has increased dramatically in recent years owing to the development and application of horizontal drilling and hydraulic fracturing techniques (Kerr, 2010; U.S. Energy Information Administration, 2013; Vidic et al., 2013). The development of these resources has dramatically altered the energy landscape, particularly in the United States (Kerr, 2010; U.S Energy Information Administration, 2013), which hosts numerous economically viable shale oil and gas plays (Chermak and Schreiber, 2014; Vengosh et al., 2013). However, hydraulic fracturing operations remain plagued by environmental concerns, namely their potential to impact surface water and groundwater quality (Brantley et al., 2014; Vengosh et al., 2013; Vidic et al., 2013). During hydraulic fracturing operations, large volumes of fracturing fluids (*i.e.*, ~8-17 million liters; Balashov et al., 2015; Chapman et al., 2012), that are often acidic and oxic (Stringfellow et al., 2014), are injected into subsurface shale formations, resulting in a system that is highly out of chemical equilibrium. It is hypothesized that disequilibrium between shale and the hydraulic fracturing fluid will induce a myriad of reactions, including mineral dissolution-precipitation, cation exchange, surface complexation, and oxidation-reduction (redox) of solid and aqueous components. Such reactions may release harmful contaminants into the environment (*e.g.,* U, Ra, As, Pb) (Balaba and Smart, 2012; Blauch et al., 2009; Chermak and Schreiber, 2014; Vengosh et al., 2014; Vidic et al., 2013). These chemical interactions may also alter the permeability and mechanical integrity of the reservoir, influencing the efficiency of production and recovery of water for re-use. Precipitation of secondary minerals and weakening and collapse of fractures due to mineral dissolution could in part be responsible for the relatively inefficient production experienced by many hydraulic fracturing operations (U.S. Energy Information Administration, 2013). However, very little is currently known about the extent to which chemical interactions between shales and these introduced fluids alter fluid and rock properties, and whether these interactions occur on a timescale relevant to hydraulic fracturing operations. Although monitoring of so-called flow-back and produced waters (waters generated following fracturing and co-produced with hydrocarbons during well operation, respectively) has revealed that the chemical composition of recovered waters differs substantially from that of the injected fluid, the controls on the evolving composition of the recovered fluids is not fully understood, and may reflect a combination of factors including mixing of injected and formation fluids and fluid-rock interaction (Barbot et al., 2013; Haluszczak et al., 2013; Lester et al., 2015; Orem et al., 2014; Renock et al., 2016; Rowan et al., 2015; Shih et al., 2015; Ziemkiewicz and He, 2015; Zolfaghari et al., 2016). Experimental investigation is required to better define the reactions that are likely to occur upon exposure of shales to hydraulic fracturing fluids and their kinetics to assess the potential contribution of fluid-rock interaction to the chemistry of produced waters and alteration of shale mechanical properties.

We investigated the types and relative rates of reactions occurring between shales of different chemical and mineralogical compositions and a simulated hydraulic fracturing fluid using a series of batch reactor experiments. Shale samples from four different oil or gas shale reservoirs with unique mineralogical compositions were used, including carbonate mineral-rich rocks from the Eagle Ford (South Texas) and Green River (Colorado) formations, and comparatively carbonate mineral-poor rocks from the

Barnett (Central Texas) and Marcellus (New York) formations, all in the United States. Currently, hydrocarbon production via hydraulic fracturing operations is ongoing for the Eagle Ford, Barnett, and Marcellus formations. Green River shale is an oil-bearing formation that, while not presently being exploited, has unique mineralogy that provides an informative contrast to the other shales under investigation. The objectives of this study were to: (1) identify the key geochemical reactions that occur upon exposure of oil or gas-bearing shales to hydraulic fracturing fluids and their kinetics, (2) elucidate the impact of initial shale mineralogy on the evolution of rock and fluid compositions during hydraulic fracturing operations, (3) evaluate the potential for release of metal contaminants to flowback and produced waters, and (4) assess reaction-induced alterations of shale porosity. The evolution of fluid composition was tracked with time, and the physical and chemical alteration of the shales was investigated post-reaction using a combination of x-ray diffraction, x-ray fluorescence spectroscopy, and scanning electron microscopy.

2. Methods

2.1 Experimental methods

The impacts of initial mineralogical composition and texture on the evolution of shale reservoir geochemistry following injection of hydraulic fracturing fluid were investigated using batch reactor experiments. A schematic of the experimental design and further detail regarding experimental methods and analytical techniques are provided in the Supporting Information (SI). Experiments were conducted for three weeks (referred to as “short-term” experiments), three months (“intermediate-term”), and six months ("long-term"). The short-term experiments were representative of the typical duration of fluid injection for hydraulic fracturing, whereas the intermediate- and long-term experiments were designed to investigate the interactions that may occur between the shale reservoirs and unrecovered fracturing fluid over longer timescales after initial fracturing operations are complete. In excess of 50% of the injected hydraulic fracturing fluid is estimated to remain in the subsurface where it may continue to react with the rock (Balashov et al., 2015; Roychaudhuri et al., 2013).

All experiments were conducted at Marcellus reservoir-representative temperatures (80°C; Renock et al., 2016; Rowan et al., 2015) and circum-atmospheric pressure in unstirred borosilicate glass serum vials. The use of circum-atmospheric rather than reservoir pressures will cause minor differences in solubility between experimental and field conditions, but the types of minerals that dissolve and their relative rates of dissolution are not expected to be strongly impacted by differences in pressure. Moreover, the impacts of pressure on solubility are small compared to temperature effects (Morel and Herring, 1993). Shale samples from four different oil and/or gas-bearing geological environments representing a wide range of clay and carbonate mineral contents were exposed to simulated hydraulic fracturing fluid (SI Figure S1). These shale samples included the Marcellus (M) gas shale (Oatka Creek Member, New York), the Eagle Ford (EF) oil/gas shale (South Texas), the Barnett (B) gas shale (Central Texas), and the Green River (GR) oil shale (Mahogany Ledge Member, Colorado). The GR and M shales used were outcrop samples collected in August 2015, and July 2016, respectively. EF and B samples were core samples taken at depth (3915 m and 2613 m, respectively).

The initial chemical compositions of the shale samples were quantified using x-ray fluorescence spectroscopy (XRF) by Jew et al. (*in press*) for the exact same GR, EF, B, and M samples used in our experiments and are tabulated in Table 1. Semi-quantitative analysis of initial mineralogical compositions was also conducted by Jew et al. (*in press*) using x-ray diffraction (XRD) data (Table 2). Peak identification was accomplished by matching the four most intense diffraction peaks for a given mineral to diffraction patterns in the National Institute of Standards and Technology (NIST) database. Semi-quantitative analysis was conducted by least squares fitting of the diffraction patterns using the NIST diffraction pattern of reference compounds with the software, JADE (Materials Data, 2002). Although these data are semi-quantitative, they are in good agreement with previously reported mineralogical compositions for these shales (Ali and Hascakir, 2015; Chalmers et al., 2012; Chermak and Schreiber, 2014).

For the purposes of this study, we separate the shales into “carbonate-rich” or “carbonate-poor” categories depending on their mineralogical and chemical compositions prior to reaction. Carbonate-rich shales contained >50 wt.% carbonate minerals, and carbonate-poor shales contained <15 wt.% carbonate minerals. The Green River and Eagle Ford samples are therefore designated carbonate-rich, and the Barnett and Marcellus samples designated carbonate-poor. The composition of the simulated fracturing fluid used in the experiments was formulated based on fluid compositions typically employed in hydraulic fracturing operations conducted in the Marcellus shale, and mimics that used in the National Energy Technology Laboratory's Marcellus Well E in Greene County, PA (“FracFocus,” 2016; Hammack et al., 2014). It contained 99.78 wt.% MilliQ distilled, de-ionized water, 0.13 wt.% hydrochloric acid, 0.03 wt.% guar gum, 0.02 wt.% ethylene glycol, 0.02 wt.% kerosene, 0.02 wt.% polyethylene glycol, 5.07×10^{-4} wt.% 2-ethylhexanol, and 1.73×10^{-4} wt.% glycol ether. During hydraulic fracturing operations, all additives are not added simultaneously, but follow a specific sequence. The experimental fluid represents a mixture of the relative proportions of these in a single solution. The initial fluid had a pH of 2.0 and was assumed to be at equilibrium with laboratory pO_2 (~0.21 atm), consistent with the injection of surface waters during hydraulic fracturing operations. A major difference between the experimental fluids and field conditions is that fluids in the field tend to have much higher total dissolved solids (TDS). A high TDS fluid was not used in the experiments for a number of reasons. First, high initial concentrations of anions like SO_4^{2-} and cations like Mg and Ca make it difficult to accurately assess changes in aqueous concentrations due to dissolution-precipitation reactions, and to conduct mass balance calculations to assess the cycling of elements in the reactors. Second, a high TDS fluid may itself alter the rate of mineral dissolution-precipitation reactions compared to published rate data from laboratory experiments conducted at more moderate TDS. This complicates the direct assessment of the impact of the hydraulic fracturing fluid additives on these mineral dissolution-precipitation reactions, as deviations from published data could be due to the high TDS rather than the fracture fluid additives. In addition, high TDS complicates the calculation of aqueous speciation. Finally, fracturing fluids are injected into shale formations at a high rate, displacing and diluting pre-existing formation fluids. This is typically followed by “shut-in” of a well for days to months prior to flowback. The critical fracturing fluid-shale reaction time is hours to days. Under such conditions, the chemistry of the fracturing fluid will dominate in fracture spaces, and formation fluids may be less important. Therefore an assessment of direct shale-fracturing fluid reactions is required.

Approximately 1 g of shale that had been pulverized to between 150 and 250 μm diameter was used in each reactor, with 200 mL of solution and ~85 mL of gas-filled headspace with the composition of the laboratory atmosphere. Although the reactors were sealed, limited replenishment of O_2 throughout the experimental duration was facilitated through semi-permeable butyl rubber septa and periodic penetration of the septa with a needle during sampling. A control experiment that lacked shale was conducted for each experimental run time. All reactors contained an α-Al_2O_3 chip (< 0.05 g) that was meant to serve as a substrate to facilitate precipitation of secondary phases. However, this substrate was found to be ineffective for this purpose. Fluid samples were taken periodically to track pH and cation and anion concentrations. Concentrations of Mg, Ca, Fe, and Si, were measured using inductively coupled plasma optical emission spectroscopy (ICP-OES). Concentrations of Al, Pb, U, Sr, and Ni were measured using inductively coupled plasma mass spectrometry (ICP-MS), and sulfate concentration was measured using ion chromatography (IC). Solids were collected post-reaction and were stored under vacuum in a desiccator prior to analysis with XRD, and scanning electron microscopy (SEM) coupled with energy-dispersive spectroscopy (EDS). Measurements of iron speciation in fluids and solids in our experiments are beyond the scope of the present study, and are instead presented in detail by Jew et al. (*in press*).

2.2. Speciation calculations

To evaluate the stability of mineral phases in the presence of the fracturing fluid, and the potential for secondary phase formation, speciation calculations were conducted using experimental pH and cation and sulfate concentration data and the geochemical modeling software, PHREEQC V.3 (Parkhurst and Appelo, 2013) with the Lawrence Livermore National Laboratory (LLNL) database. Owing to the dearth of available thermodynamic data to represent the fracture fluid additives, only the additive HCl was included in the models; the organic additives were neglected. Speciation calculations may therefore overestimate the saturation state of mineral phases if significant complexation of inorganic ions with fracture additives or organic complexes native to the shale samples occurred. It should also be noted that speciation calculations assumed equilibrium between aqueous Fe(II) and Fe(III), despite potential kinetic limitations to aqueous Fe(II) oxidation at low pH (Morgan and Lahav, 2007). Due to a lack of dissolved inorganic carbon (DIC) data, DIC concentrations were assumed to reflect primarily carbonate dissolution and were therefore set to balance dissolved Ca concentrations assuming stoichiometric calcite dissolution, as calcite was determined to be the main source of Ca and the most reactive carbonate phase in the samples (refer to section 3.2.3).

3. Results and Discussion

Predictions about the effects of the reaction of hydraulic fracturing fluid with shale on contaminant release, fracturing fluid transport, and hydrocarbon recovery requires identification of the types of reactions that will occur as well as their kinetics. However, the complex mineralogy of shales, the commonality of elements between minerals, and the possibility of incongruent dissolution and secondary mineral precipitation confound the direct attribution of aqueous solute concentrations to specific mineral dissolution-precipitation reactions. To address this, we use multiple lines of evidence to determine the mineral dissolution-precipitation reactions that are most likely to occur over the typical timescale of hydraulic fracturing operations (weeks to months) as well as the shale components that govern the evolution of fluid composition and rock porosity and permeability.

3.1 Evolution of fluid composition

3.1.1. Calcium, magnesium, and pH

Of the major elements initially present in the shales, Ca was released into the fracturing fluid to the greatest extent. In all experiments the release of Ca was initially rapid, before plateauing at reasonably stable values within 48 h (Figure 1a). The steady-state Ca concentrations differed among the four shales and did not correspond directly to the Ca content of the solid phases. The highest aqueous Ca concentration was recorded for the EF shale, followed by the M, the GR, and finally, the B shales (Figure 1a). Yet, the initial solid Ca content of the GR shale exceeded that of the M shale (Table 1). The maximum aqueous Ca values during three weeks of reaction were EF (318 mg L^{-1}), M (242 mg L^{-1}), GR (221 mg L^{-1}), and B (192 mg L^{-1}) (Figure 1a). Aqueous Ca concentrations remained relatively stable in both the intermediate- and long-term experiments (Figure 2a), indicating that the majority of Ca release occurred within 48 h. Different Ca concentrations (up to ~30% different) were observed between duplicate M reactors in both the intermediate- and long-term experiments, which is attributed to mineralogical heterogeneity of the starting solids (Figure 2a). Small differences in Ca concentration trends between the short-term Barnett duplicates are also attributed to heterogeneity of the initial solids. The Marcellus exhibited a large degree of heterogeneity visible at the millimeter scale (SI Figure S2). The smaller degree of heterogeneity in the Barnett samples compared to the Marcellus samples is attributed to different sampling protocols; the Barnett was sampled from core, whereas the Marcellus was sampled from outcrop.

Trends in Mg release to solution were similar to those observed for Ca for the GR, M, and B shales, with a rapid initial increase within 48 h, followed by relatively stable concentrations for the remainder of the short-term experiments (SI Figure S3). However, maximum aqueous Mg concentrations were lower than Ca solution concentrations, with less than 50 mg L^{-1} Mg for all four shales. This is consistent with the lower solid phase Mg content for all shales (Table 1). Similar to Ca, Mg concentrations remained relatively stable for the durations of the intermediate- and long-term experiments for the GR, M, and B shales, suggesting that the majority of Mg release also occurred within the first 48 h of reaction (SI Figure S3). Although Mg content in the initial shale material for EF was similar to B and M (Table 1), the total concentration of Mg in solution was significantly lower (< 3 mg L^{-1}) in the short- and intermediate-term experiments, and remained below quantifiable limits for the long-term experiment (*i.e.*, <1 mg L^{-1}).

In all experiments the rapid increases in Ca concentrations within 48 h coincided with rapid increases in solution pH (Figure 1a,b). In fact, two distinct trends in fluid pH were evident in the experiments as a function of the initial carbonate mineral content of the rock. The carbonate-rich EF and GR shales exhibited rapid pH increases from values of ~2 before plateauing at circum-neutral values within 48 h, which coincided with plateaus in Ca concentration (Figure 1b). The pH was maintained at circum-neutral levels throughout the durations of the intermediate- and long-term carbonate-rich shale reactors (Figure 2b). Conversely, the pH for the carbonate-poor B and M reactors remained acidic, plateauing at values between 3 and 5 for experiments of all durations up to six months (Figures 1b and 2b). Differences in fluid pH between duplicate reactors were documented for the intermediate- and long-term M reactors, as was observed for Ca concentrations and was attributed to sample heterogeneity (Figure 2b). The experiments with higher pH corresponded to those with higher Ca concentrations.

3.1.2. Iron release

All Fe concentrations reported represent total aqueous Fe as measured with ICP-OES. Iron concentrations were too low to be quantified using our analytical techniques for the GR and EF shales in reactors of all timescales (<~0.3 ppm). Aqueous Fe concentrations for both the M and B shales, on the other hand, increased rapidly within ~200 h. Fe concentrations reached up to 27 mg L^{-1} in the M reactor and 17 mg L^{-1} in the B reactors, after which Fe concentrations declined for both B and M (Figure 1c). However, Fe concentrations did not decline over time in the intermediate- or long-term B reactors. Rather, they oscillated at ~20 mg L^{-1} for the majority of the intermediate-term reactor and exhibited a gradual increase to 37 mg L^{-1} in the long-term reactor (Figure 2c). As observed for Ca concentrations, duplicate M shale reactors exhibited different Fe concentrations in both the intermediate- and long-term experiments (Figure 2c). Iron concentrations oscillated between 12 and 32 mg L^{-1} in one intermediate-term experiment, but remained below 14 mg L^{-1} in the duplicate experiment. A more pronounced difference was documented for the long-term experiments; the Fe concentration continued to gradually increase throughout the experimental duration in one reactor, reaching up to 37 mg L^{-1}, whereas the Fe concentration was fairly stable between 3 and 6 mg L^{-1} for the duplicate experiment (Figure 2c).

3.1.3. Sulfate release

Unlike the decline observed for Fe, aqueous SO_4^{2-} concentrations increased throughout the short-term B and M experiments (Figure 1d). Similarly, in the short-term EF experiment, SO_4^{2-} concentrations increased throughout the experimental duration, despite the lack of measurable Fe in solution. In the GR reactors, on the other hand, aqueous SO_4^{2-} concentrations remained below quantifiable values. This is a consequence of the minimal pyrite in this shale. The differences observed for the concentrations of other elements (Ca, Fe) and pH between duplicate M experiments were less pronounced for SO_4^{2-}. The SO_4^{2-} concentrations were similar between duplicate M intermediate-term reactors, and stabilized after 722 h between 134 and 147 mg L^{-1}. In the long-term experiments, SO_4^{2-} concentrations stabilized within 966 h, plateauing at ~140 mg L^{-1} in one reactor and ~170 mg L^{-1} in the other reactor (Figure 2d). A similar extent of sulfate release was observed for the long-term compared to the intermediate-term experiments for all shales, except for the EF, for which a maximum of 98 mg L^{-1} SO_4^{2-} was measured in the intermediate-term compared to 141 mg L^{-1} in the long-term experiment (Figure 2d).

Pyrite was the only S-bearing phase detected with XRD (Table 2), therefore its release to solution is attributed primarily to pyrite dissolution. Mass balance calculated with respect to the XRF-measured sulfur content of the initial solids and final aqueous SO_4^{2-} concentrations revealed that approximately 38%, 37%, 39%, and 36% of the total initial pyrite mass was oxidized within three weeks of reaction in the EF, M, and duplicate B experiments, respectively (SI Figure S4). The extent of pyrite oxidation remained less than 55% in all intermediate- and long-term EF, M, and B experiments, except for the long-term EF experiment, for which up to 72% of pyrite was calculated to have been reacted (SI Figure S4). In all cases, the majority of pyrite oxidation occurred within the first three weeks of exposure to the simulated fracturing fluid. This result implies that the injection of oxic fracturing fluids will induce oxidative dissolution of pyrite, releasing Fe and SO_4^{2-} into produced waters on a timescale of hours to weeks.

3.1.3. Aluminum and silicon

The experiments were conducted in borosilicate reactors and contained Al_2O_3 substrates; these could release Si and Al to solution. The extent of dissolution of these components of the reactors was assessed by comparing Si and Al concentrations in the controls that lacked shale to reactors that contained shale. There was negligible Al and Si release in the short-term controls, confirming that changes in Al and Si concentrations in the short-term experiments are attributable to reaction of shale components. However, in the intermediate- and long-term experiments, Al and Si concentrations in most reactors were not substantially different from those measured in the control experiments. Therefore Si and Al cycling occurring in these experiments due to reaction of the shale components alone cannot be assessed, and further discussion is limited to the short-term experiments.

There was very little net mass transfer of Al and Si from the solid to fluid phase in the short-term reactors (Figure 3c). The greatest extent of Si release in the short-term reactors was documented for the GR shale, reaching 16 mg L^{-1}, whereas similar concentrations of <10 mg L^{-1} were documented for the other three shales (Figure 3a). Al was released to the greatest extent from the Marcellus and Barnett shales, but nevertheless remained below 3 mg L^{-1} in all short-term reactors (Figure 3b). This is consistent with the known slow dissolution rates of the silicate minerals present in these shales (Palandri and Kharaka, 2004).

3.2 Identification and kinetics of key reactions

3.2.1 Iron cycling reactions

The presence of multiple Fe-bearing phases of varying, and often poorly-constrained reactivity in shales (Carroll et al., 2013), and the array of secondary Fe-bearing minerals that can form (*e.g.*, goethite [FeO(OH)], hematite [Fe_2O_3], amorphous $Fe(OH)_3$; Blowes et al., 1998; Nordstrom, 1982), complicates attribution of the sources of dissolved Fe and the prediction of its fate. The potential sources of dissolved Fe in the four shales include Fe-bearing carbonate minerals (siderite or $(Mg\text{-}Ca\text{-}Fe)_xCO_3$ solid solutions), clays (illite, smecite, and chlorite-group minerals), organic matter, and pyrite. The low extent of Si and Al release in all experiments is consistent with the relatively slow dissolution rates of aluminosilicate minerals compared to carbonate minerals and pyrite (*i.e.*, $10^{-5.81}$ mol/m^2/s, $10^{-4.55}$ mol/m^2/s, $10^{-9.12}$ mol/m^2/s, and $10^{-12.78}$ mol/m^2/s for calcite, pyrite, anorthite, and smectite, respectively, at 25°C and neutral pH; *c.f.*, Palandri and Kharaka, 2004; Golubev et al., 2009; Rimstidt and Vaughan, 2003; Smith et al., 2013), and suggests that the dissolution of clays was not the main contributor of dissolved Fe in the experiments. Rather, the substantial increase in aqueous SO_4^{2-} concentration in all experiments with pyrite-bearing shales (EF, B, and M) indicates that dissolution of pyrite was an important control on Fe release. The GR shale used in the experiments lacked detectable pyrite based on XRD characterization, although minor pyrrhotite [$Fe_{(1-x)}S$] was detected with

XRF mapping (Jew et al., *in press*), and neither dissolved Fe nor SO_4^{2-} reached quantifiable concentrations in these reactors.

Pyrite is interpreted to be the main source of aqueous SO_4^{2-}, therefore deviation of Fe:SO_4^{2-} molar ratios from stoichiometric pyrite values (0.5) are indicative either of secondary phase precipitation, which preferentially removes one element over the other, or dissolution of other Fe-bearing minerals. The Fe concentrations that would be produced from stoichiometric pyrite dissolution based on measured SO_4^{2-} concentrations were calculated for all pyrite-bearing shales (Figures 1c and 2c). Measured Fe concentrations that are less than calculated Fe concentrations are indicative of precipitation of Fe-bearing phases, whereas measured Fe concentrations that are greater than calculated values indicate either precipitation of SO_4^{2-}-bearing phases or an additional source of Fe in the experiments (*e.g.*, siderite dissolution). For M shale, Fe concentrations declined below stoichiometric values after 200 h in the short-term experiments and remained significantly lower (>8 mg L^{-1} lower) than stoichiometric throughout the durations of the intermediate- and long-term experiments (Figures 1c and 2c). Similarly, Fe concentrations were below detection for the EF experiments, yet stoichiometric pyrite dissolution would generate up to 26, 28, and 48 mg L^{-1} Fe in the short-, intermediate-, and long-term experiments, based on SO_4^{2-} concentrations. The oxidative dissolution of pyrite is commonly accompanied by precipitation of secondary Fe(III)-bearing (hydr)oxide phases (Blowes et al., 1998; Nordstrom, 1982), and speciation calculations revealed that amorphous $Fe(OH)_3$ became supersaturated in M reactors within 24 h (Figure 4a). Moreover, rust-colored precipitates were observed in suspension and coating the walls of the reactors for both the M and B experiments of all durations, suggesting the presence of oxidized Fe-bearing secondary phases (SI Figure S5). Though the lack of aqueous Fe data for the EF experiments precludes direct calculation of the saturation indices of Fe-bearing minerals, the Fe concentration necessary to saturate the fluid with respect to amorphous $Fe(OH)_3$ in these experiments is sufficiently low such that the solutions may have been saturated with respect to this phase without measurable Fe concentrations. The removal of iron from solution relative to sulfate in both the M and EF experiments is thus inferred to reflect the precipitation of secondary Fe(III)-(oxy)hydroxide phase(s). Similarly, the observation of rust-colored precipitates coating reacted GR particles indicates that Fe(III)-bearing precipitates were also formed in these experiments (SI Figure S5), despite the lack of pyrite. Pyrrhotite was identified with synchrotron-based XRF mapping at low abundance and as the main host of Fe in these samples before reaction (Jew et al., *in press*), suggesting pyrrhotite rather than pyrite dissolution may have been the source of Fe in the GR experiments. Fe(III)-bearing precipitates were not present in sufficient quantities in any of the experiments to identify with XRD.

In contrast to the M and EF, the B exhibited greater Fe release than can be attributed to stoichiometric pyrite dissolution within the first 100 h of reaction, and in the intermediate- and long-term B experiments, Fe concentrations remained in excess of those predicted by stoichiometric pyrite dissolution for the majority of the experimental durations (Figures 1c and 2c). The rapid increase in Fe concentration relative to sulfate at the beginning of the experiments implies that a mineral with a rapid dissolution rate, such as siderite or Fe-bearing calcite, was also contributing Fe to solution. This implication could also result in excess Fe concentrations compared to stoichiometric pyrite dissolution in the longer-term experiments. Alternatively, precipitation of S-bearing phases could produce the apparent excess in Fe concentration, and would also serve to clog pore spaces. Speciation calculations revealed that Ca-sulfate minerals were not saturated in the bulk solution, yet precipitates containing Ca, S, and O were identified with SEM and EDS in B samples from the long-term experiments (SI Figures S6 and S7). As such, it is not certain whether these precipitates formed *in situ* during the experiments, or were an artifact formed when the samples were dried following the experiment. If formed during the experiments, these precipitates could account for the excess Fe in solution with respect to stoichiometric pyrite dissolution. However, following the initial rapid release, Fe concentrations in the short-term B experiments declined below stoichiometric values for pyrite dissolution after 95 h (Figure 1c), which is again attributed to the formation of Fe(III)-(oxy)hydroxide. Similarly, the lack of measurable aqueous Fe throughout the EF and GR experiments and the decline in Fe concentration after 95 h in the M experiment implies that precipitation of Fe(III)-(oxy)hydroxides began at least within 95 h in these experiments. This conclusion suggests precipitates could form within hours of hydraulic fracturing and could have significant consequences on the transport and recovery of hydrocarbons and the compositions of flowback and produced waters.

3.2.2. Controls on pyrite oxidation

The dissolution of pyrite from oil and gas shales is of concern, as it is known to release trace metal contaminants, including As, Pb, and Hg (Rimstidt and Vaughan, 2003); therefore, it is important to constrain the extent of pyrite reaction that may occur upon injection of oxidized fracturing fluids into shales. In our experiments, the incomplete reaction of pyrite (SI Figure S4) indicates that its dissolution became inhibited over time. There are a number of potential explanations for the apparent inhibition of pyrite dissolution, including: (i) passivation of pyrite surfaces due to precipitation of secondary minerals as surface coatings (Nicholson et al., 1990), (ii) exhaustion of the $O_{2(aq)}$ supply in the reactor, as O_2 is required for oxidative pyrite dissolution, or (iii) pyrite grains located near the surface of the shale particles were consumed at early times, leaving the remaining pyrite within the interior of shale particles poorly exposed to the reactive fluid. This latter possibility is dismissed, as numerous pyrite grains exposed on the surfaces of reacted shale particles were observed with SEM. On the other hand, because the oxidation of pyrite, aqueous Fe(II), and other redox-active components consumes O_2 (Eqs. 1 and 2), the dissolution of pyrite may be self-limiting due to the removal of O_2 as a reactant.

$$FeS_2 + 3.5O_2 + H_2O \leftrightarrow Fe^{2+} + 2SO_4^{2-} + 2H^+ \quad (1)$$

$$Fe^{2+} + 0.25O_2 + H^+ \leftrightarrow Fe^{3+} + 0.5H_2O \quad (2)$$

Using the initial O_2 content of the reactors as a lower limit to the amount of O_2 available, and assuming the reaction stoichiometry in equations 1 and 2 and no additional O_2-consuming reactions, mass balance calculations reveal that there was sufficient oxygen present to facilitate further pyrite reaction in all experiments, except perhaps one long-term M reactor (SI Figure S4). Moreover, the semi-permeable nature of the butyl rubber stoppers facilitated some replenishment of O_2 from the laboratory air. Conversely, the precipitation of Fe-(oxy)hydroxides was inferred from fluid compositions (section 3.2.1.). This inference implies that the incomplete reaction of pyrite in the experiments is more likely attributable to passivation of the pyrite surface via precipitation of Fe-(oxy)hydroxide phases as surface coatings than to a lack of O_2.

Although the availability of O_2 was not limiting for pyrite reaction in the experiments, this may not be the case at field scale during hydraulic fracturing operations due to the highly reducing conditions of shale reservoirs, and the higher rock to O_2 ratio than used in our experiments. For example, during a typical hydraulic fracturing operation in the Marcellus shale, approximately 1.7×10^4 m^3 of oxygenated fracturing fluid may interact with ~1.5×10^7 m^3 of shale (Balashov et al., 2015). Assuming the same pyrite abundance as in the Marcellus experiments and initial equilibrium of the fluid with respect to atmospheric pO_2, these estimates imply a dissolved O_2 to pyrite molar ratio of 3.7×10^{-7}, which is far less than that required to completely oxidize the pyrite (*i.e.*, a ratio of 3.5; Eq. 1). Only 1.0×10^{-5}% of the pyrite would be oxidized under this scenario, implying a similarly low percentage of release of trace metals via its dissolution, if dissolution were to occur stoichiometrically. This suggests that at the scale of typical hydraulic fracturing operations, the amount of pyrite oxidation that can occur will be limited by the O_2 supply when the fluid is imbibed into the matrix. If the fluid is not imbibed to a great extent, the reaction may occur mainly at the fracture-matrix interface, where the supply of O_2 could still be excessive. Similarly at grain scale, the precipitation of Fe-(oxy)hydroxides as surface coatings on pyrite may severely limit the reaction rate of individual pyrite grains, effectively stopping pyrite oxidation. In either case, the magnitude of release of contaminants such as Pb from pyrite dissolution will be governed in part by the amount of oxygen injected into the subsurface, which is a function of the concentration of dissolved oxygen in and the volume of the fracturing fluid injected, and the degree to which this fluid is imbibed into the matrix. The rock:fluid ratios are high in the subsurface, thus even the reaction of a small proportion of reactive phases like pyrite at the fracture-fluid interface may strongly alter the fluid composition.

3.2.3. Dissolution of carbonate minerals

There are a number of minerals in all of the shales that could dissolve to release Ca and Mg to solution, including the carbonate minerals calcite [$CaCO_3$] and dolomite [$Ca,Mg(CO_3)_2$], illite, smectite, and chlorite-group clay minerals, and plagioclase feldspar (Ca-endmember anorthite [$CaAl_2Si_2O_8$]). Dissolution of carbonate minerals is rapid compared to dissolution of aluminosilicate minerals, and calcite dissolution in particular is rapid compared to dolomite dissolution (Palandri and Kharaka, 2004; Pokrovsky et al., 2005). The relatively low degree of Si and Al release in these experiments compared to Ca is consistent with the large differences in dissolution rates of Ca-bearing minerals, and implies that aluminosilicates were not the primary source of dissolved Ca in these experiments. Dissolution of carbonate minerals, on the other hand, is rapid and provides alkalinity to solution. Thus, the coincidence of rapid Ca release rates and rapid pH increases are consistent with Ca-carbonate mineral dissolution as the main source of dissolved Ca in these experiments. Analysis of the shales following reaction with XRD confirmed a reduction of calcite content in all shales, whereas the abundances of dolomite and clays were less altered (Jew et al., *in press*). We conclude that calcite dissolution was the primary source of dissolved Ca for both carbonate-poor and carbonate-rich shales. However, the occurrence of plateaus in Ca concentration and the magnitude of Ca concentration at these plateaus are attributed to different factors for the carbonate-rich compared to the carbonate-poor shales.

Speciation calculations revealed that coincident Ca concentration and circum-neutral pH plateaus for the carbonate-rich shales (EF and GR) are associated with achievement of equilibrium with respect to calcite (Figure 5); the fluid reached saturation with respect to calcite within 48 h and remained approximately at equilibrium throughout the remainder of the short-term experiments. Similarly, throughout the intermediate- and long-term EF and GR experiments, fluids remained approximately at equilibrium with respect to calcite. In contrast, for the carbonate-poor B and M shales, the solutions remained undersaturated with respect to calcite for experiments of all durations (Figure 5). Mass balance calculations based on bulk XRF analysis of the initial materials and final aqueous Ca concentrations revealed that these carbonate-poor shales were almost completely stripped of Ca within three weeks, whereas the carbonate-rich EF and GR shales maintained more than 70% of their initial Ca over the same time period (inset Figure 1a). The plateaus in Ca concentration and pH are attributed to the exhaustion of the accessible calcite for the carbonate-poor shales, and to the achievement of equilibrium with respect to calcite for the carbonate-rich shales. The magnitude of the Ca concentration at these plateaus is therefore dictated by the mass of fluid-accessible calcite for the carbonate-poor shales, and the extent of dissolution required to achieve equilibrium for the carbonate-rich shales. The concentration of Ca and fluid pH at equilibrium with respect to calcite will differ slightly between the experiments and field conditions due to the lower pressure used in the experiments.

Calcite dissolution generates alkalinity, yet the oxidative dissolution of pyrite generates acidity. Both reactions were documented to occur on a similar timescale in all experiments with pyrite-bearing shales. The pH of the fluid at which the pH values plateau therefore reflects the balance between the extent of pyrite dissolution and the abundance of calcite available to the buffer the fluid pH. In the case of the carbonate-poor shales (B and M), fluids remained acidic as there was insufficient calcite available to counterbalance the combined acidity of the initial fracturing fluid and that generated from pyrite oxidation. Conversely, the carbonate-rich EF and GR shales had sufficient alkalinity-generating capacity to neutralize all acidity. The extent of calcite dissolution that occurs in a shale formation will therefore depend on the initial pH and volume of the injected fluid, as well as the abundance of pyrite in the shale and amount of dissolved oxygen in the injected fluids.

Notably, dolomite, another fairly abundant carbonate mineral in these shales (Table 2), remained undersaturated in the B and M experiments, was close to equilibrium in the short- and intermediate-term EF experiments, and was slightly supersaturated in the GR experiments (SI Figure S8). The saturation state of siderite [$FeCO_3$] could not be calculated for the EF and GR experiments due to the lack of aqueous Fe concentration data, but it remained undersaturated in the B and M experiments. This finding implies that although dissolution of these other carbonate minerals likely occurred, calcite exerted the strongest control on overall fluid pH and Ca concentrations. The low Mg concentrations documented in the EF shale experiments indicate little dolomite dissolution occurred, despite the solutions approaching equilibrium with respect to dolomite. The similar temporal trends in aqueous Mg compared to Ca indicate it was likely sourced from the dissolution of Mg-bearing calcite for the B and M shales.

3.3 Alteration of porosity

3.3.1. Porosity generation

Discrete holes of size similar to intact calcite grains in unreacted material (10s of microns) were observed post-reaction in the B shale for all experimental durations (Figure 6). These holes are attributed to the preferential dissolution of calcite. The generation of large, isolated pores was not observed for the M shale, despite the removal of the majority of the calcite from this shale (Figure 6). This result is attributed to differences in initial calcite distribution and size between the two carbonate-poor shales; the calcite in the M was distributed as clusters of smaller grains (<10 μm), compared to generally larger (~15-50 μm), isolated grains in the B (SI Figures S9 and S10). In the EF shale, calcite was also generally distributed as large, isolated grains (SI Figure S11). Changes in surface morphology of the EF were not broadly evident, but some particles did exhibit a mottled texture indicative of porosity generation (Figure 6).

Unlike the other shales, calcite was distributed as pervasive cement that filled the areas between silicate and dolomite grains in the GR shale (SI Figure S12). The preferential dissolution of this calcite cement generated a mottled, spongy texture over the majority of the GR shale surface, consistent with the generation of a porosity network (Figure 6). We inferred from aqueous compositions that ~30% of the calcite was lost from the GR shale. Assuming uniform reaction, this translates to a reaction front penetrating ~42 μm deep in each GR particle, and approximately a 1.5-fold increase in the total estimated bulk pore volume of the particles (initial porosity estimated at 10%; Law et al., 1986). Although the secondary porosity network did not appear to be as uniform in the other shales, the calculated bulk pore volume increase for the entire shale mass of each type was similar. The increase in bulk pore volume was estimated to be 3.0-, 2.2-, and 3.4-fold for the B, EF, and M shales, respectively, based on mass balance estimates of calcite loss, and initial porosity values of 3%, 9%, and 4%, respectively (Chalmers et al., 2012; Jennings and Antia, 2013; Law et al., 1986).

Our experiments reveal that the interaction of the calcite-bearing shales with acidic fracturing fluid will generate porosity due to calcite dissolution, but the connectivity and distribution of this porosity is dictated by the pore-scale distribution of calcite. Isolated calcite grains tended to generate discrete pores, whereas more homogeneous calcite distribution appeared to result in a more pervasive secondary porosity network. It is well known that even minor changes in porosity can profoundly influence the permeability of a rock (Andreani et al., 2009; Gouze and Luquot, 2011; Luquot et al., 2012; Luquot and Gouze, 2009; Smith et al., 2013), but the net effect of the generated porosity on fluid transport in these shales requires further investigation. It is possible that secondary porosity could enhance the transport of hydrocarbons across the matrix-fracture interface by increasing permeability. Alternatively, hydrocarbon and fluid transport could be inhibited due to capillary effects or weakening of the shale matrix and the subsequent collapse of fractures and large pores. The higher pressure in shale formations compared to our experiments is likely to exert a strong control on the importance of these porosity-altering reactions on permeability, and the imbibition of the fluid into the matrix, which requires further investigation. The manner in which permeability evolves under stress is impacted by shale mineralogy; clay-rich shales tend to exhibit greater pore-throat compressibility (Al Ismail and Zoback, 2016). Therefore the observed geochemical reactions may alter the response of shale permeability to the stresses experienced during hydraulic fracturing due to changes in composition and distribution of pore types and sizes. Regardless, our experiments reveal that geochemical reactions have the potential to alter porosity, and the manner in which it is altered will depend not only on the abundance, but also on the distribution of highly reactive phases such as calcite.

3.3.2. Porosity occlusion

3.3.2.1 Fe(III)-bearing precipitates

Pyrite is the main source of aqueous Fe and SO_4^{2-} from the M and EF shales, thus the deficit between measured Fe concentrations and those expected for stoichiometric pyrite dissolution can be used to approximate the volume of Fe-(oxy)hydroxide precipitated. In the B experiments, an additional source of Fe precludes simple mass balance calculation. In the case of the M and EF, the main reaction product is inferred to be amorphous $Fe(OH)_3$ in the short-term experiments. Assuming a density of ferrihydrite (3.96 g/cm^3; Jambor and Dutrizac, 1998), the volume of $Fe(OH)_3$ precipitated is only ~4% and 6% of the pore volume generated via calcite dissolution for the EF and M shales, respectively. Despite the reddish coloration observed in the reactors, Fe-(oxy)hydroxides were not observed with SEM, which is consistent with the calculated low volume of precipitates. Thus, calcite dissolution appears to have more strongly influenced the evolution of porosity than did precipitation of secondary phases. Nevertheless, depending on the location in which precipitates form, for example in pore throats versus large pores, they may exert an important control on the transport properties of the rock even with a small volume precipitated (Andreani et al., 2009; Gouze and Luquot, 2011; Luquot et al., 2012; Luquot and Gouze, 2009; Smith et al., 2013). The formation of Fe(III)-precipitates requires the oxidation of both pyrite and aqueous Fe(II), and therefore the total volume of precipitates that can form will be limited by the amount of oxidizing agents that are injected, particularly dissolved O_2.

Although the majority of pyrite oxidation concluded within three weeks, speciation calculations revealed that the type of Fe(III)-bearing precipitate may have changed over time during the intermediate- and long-term experiments, as is consistent with known stability of Fe(III)-(oxy)hydroxides (Cudennec and Lecerf, 2006; Schwertmann et al., 1999). The morphology, size, and density of the precipitates are expected to evolve during these phase transformations (Johnston and Lewis, 1983; Michel et al., 2010), therefore porosity and permeability may have continued to evolve due to these transformations. The crystalline phases hematite and goethite were highly supersaturated during the early stages of the reaction for both the M and B shales, whereas the saturation index of amorphous $Fe(OH)_3$ declined towards equilibrium in the short-term experiments. However, in the intermediate- and long-term B experiments, the fluids were undersaturated with respect to amorphous $Fe(OH)_3$, yet close to equilibrium with respect to hematite and goethite (Figure 4). The same was true for duplicate intermediate-term and one of the long-term M experiments. The other long-term M reactor remained close to equilibrium with respect to amorphous $Fe(OH)_3$ due to the higher pH of this reactor compared to its duplicate (data not plotted). The transition from saturation with respect to amorphous $Fe(OH)_3$ to the more crystalline Fe(III)-bearing phases suggests that the poorly crystalline precursors may have been replaced by more stable phases over time (Steefel and Van Cappellen, 1990). Although saturation indices may have been overestimated due to relatively slow aqueous Fe(II) oxidation rates (*i.e.*, not equilibrium), and complexation with organics in the fracture fluid or native to the shale that were not accounted for in the speciation calculations, phase transitions are nevertheless expected in the Fe(III)-(oxy)hydroxide system (Cudennec and Lecerf, 2006; Schwertmann et al., 1999). The reduction in porosity of a reaction layer during similar phase transformations between hydrated Mg-carbonate minerals has been postulated to severely limit reaction rates of dissolving minerals (Harrison et al., 2016, 2015). Though not directly observed in the present study, it is possible that the ripening of secondary phases in the shale-hydraulic fracturing fluid system results in continued porosity and permeability evolution over the longer term even after cessation of pyrite oxidation.

3.3.2.2. Al-bearing precipitates

Colorless, gelatinous suspended solids were observed within 6 h in all of our short-term experiments, including controls, and persisted throughout the intermediate- and long-term experiments. These solids were not successfully recovered from the short-term experiments but were selectively removed at the conclusion of the intermediate- and long-term experiments. Precipitates associated with this gelatinous substance consistently appeared as bulbous, pseudo-spherical entities as observed using SEM (SI Figure S6). EDS analysis indicated that these precipitates are composed of Al, O, and in some cases, Cl, suggesting that they are a poorly-crystalline Al-hydr(oxide) phase (SI Figure S6). Speciation calculations revealed that the Al-hydroxide phases gibbsite [$Al(OH)_3$] and boehmite [γ-AlO(OH)] became supersaturated within 100 h in all short-term experiments (SI Figure S13). The relatively constant level of supersaturation achieved with respect to these phases in the short-term experiments suggests the aqueous Al concentrations were controlled by precipitation of an amorphous Al-hydr(oxide) phase, which is consistent with the observation of amorphous Al-hydroxide flocs that form during mixing of acidic mine drainage waters with neutral surface waters (Furrer et al., 2002). The presence of these Al-bearing precipitates in the short-term experiments could account for the measured solution compositions, though their presence could not be confirmed with SEM. Like the Fe(III)-(oxy)hydroxides, these Al-hydr(oxides) provide the potential to clog pore space and fracture apertures, as well as acting as surfaces for adsorption of trace metals, should they form in the subsurface. However, both boehmite and gibbsite were undersaturated in the long-term experiments for all shales, suggesting that they may not be stable for long durations.

3.4 Contaminant and trace element release

3.4.1 Lead, uranium, and nickel

One of the major environmental concerns of hydraulic fracturing operations is the potential to contaminate ground or surface waters with toxic or radioactive metals such as As, Pb, and U initially present in the host rock reservoir (Chermak and Schreiber, 2014; Phan et al., 2015; Vengosh et al., 2014). Such contaminants can be released along with other trace elements during dissolution of shale minerals and degradation of organic matter (Jin et al., 2013; Jung et al., 2013; Phan et al., 2015; Tuttle et al., 2009; Wang et al., 2015). To assess the source and fate of contaminant metals in our shale-fracturing fluid experiments, the concentrations of U, Pb, and Ni were tracked with time. Lead is a common trace element in pyrite that can be released upon its dissolution (Rimstidt and Vaughan, 2003), whereas U in the Marcellus shale is primarily hosted in silicate minerals, with up to 20% hosted in carbonate minerals (Phan et al., 2015). Aqueous concentrations of both Pb and U remained too low for accurate measurement for all but the M shale. Nickel is a common minor element in pyrite (Rimstidt and Vaughan, 2003) that was present at higher abundance than U and Pb in the shales we examined (Table 1). Nickel concentrations were therefore tracked to provide insight as to the behavior of the typical pyrite-bound contaminants that were not successfully measured for the EF and B shales.

Nickel release from the M and B shales exhibited behavior similar to that of SO_4^{2-} in the short-term experiments, and there was negligible Ni release from the GR shale. These trends are consistent with Ni being sourced primarily from pyrite dissolution (Figure 7a,b). Declines in Ni concentration were observed in the intermediate- and long-term EF experiments, and remained relatively stable throughout the durations of the intermediate- and long-term B experiments (Figure 7a). Nickel concentrations also exhibited moderate declines in the intermediate- and long-term M experiments, and the maximum concentrations differed between duplicate reactors, as was documented for Ca, Fe, and pH (Figure 7b).

Similar to Ni, the temporal trend in aqueous Pb concentration mimicked that of SO_4^{2-} in the short-term M experiments, implying that Pb was also released from dissolving pyrite (Figure 7c). Conversely, U was released rapidly from the M shale in the first 24 h, after which its concentration continued to increase at a much slower rate, reaching a maximum of 64 µg L^{-1} in the short-term experiments (Figure 7d). This result for U is similar to the behavior of Ca and fluid pH, implying that U is primarily sourced from carbonate dissolution, which is consistent with observations of Phan et al. (2015). However, both U and Pb concentrations exhibited pronounced declines over time in one each of the duplicate intermediate- and long-term M experiments (Figures 7c,d). In the other duplicate reactors, U, and Pb concentrations remained significantly lower throughout the experimental durations (Figure 7d). The reactors with low aqueous concentrations of U, Pb, and Ni were also those for which aqueous Ca concentrations and pH were high, but Fe concentrations were low. A comparison of maximum U, Pb, and Ni concentrations versus maximum fluid pH for the M reactors of all durations reveals a tendency of lower U, Pb, and Ni concentration with higher pH (Figure 8a). Sulfate release occurred to a similar magnitude in both intermediate-term M duplicates, and sulfate concentrations were higher in the long-term duplicate experiment with lower Ni, U, and Pb concentrations, indicating that the lower aqueous concentrations of these trace elements cannot be attributed to less pyrite dissolution. Rather, like the concentrations of these trace elements, a tendency toward lower aqueous Fe:S molar ratio as a function of pH was observed in the M reactors (Figure 8b), which is indicative of a greater extent of Fe-(oxy)hydroxide precipitation in the reactors with higher pH. The removal of U, Pb, and Ni from solution likely reflects adsorption at the surface of and/or co-precipitation with these secondary (oxy)hydroxide phases, a well-known phenomenon (Bargar et al., 1997; Benjamin and Leckie, 1981; Bruno et al., 1995; Duff et al., 2002; Enid Martinez and Mcbride, 1998). This greater degree of Fe-(oxy)hydroxide precipitation is facilitated by a faster rate of aqueous Fe(II) oxidation, which increases as a function of pH (Morgan and Lahav, 2007; Stumm and Lee, 1961), and resulted in lower aqueous concentrations of trace metals for the M reactors. A similar process could account for the decline in Ni concentrations in the EF reactors, implying that trace metal contaminants may also be removed in this fashion for the EF shale. The stabilization of Ni concentrations in the longer-term experiments for the B and GR shales may indicate the cessation of dissolution of the source phase for Ni; therefore, it is not clear whether sequestration of trace metals was occurring in these experiments.

Although the formation of precipitates may serve to clog porosity and inhibit hydrocarbon recovery, they may also be beneficial due to the apparent mitigation of contaminant release. However, the transformation from less to more stable phases over time may affect the sorption capacity of the secondary phases, therefore contaminant concentrations may continue to evolve along with porosity. As both the precipitation of (oxy)hydroxides and the subsequent sorption of metals are favored at higher pH, contaminant mobility will be highly sensitive to the relative proportion of acid and alkalinity-generating reactants – namely the abundance of calcite and pyrite in the shale, and the concentration of dissolved O_2 and acidic additives present in the fracturing fluid. Higher acid concentrations and lower carbonate mineral content will tend to favor mobility of contaminants. These results imply that the contamination of flowback and produced waters will depend not only on the abundance of contaminants in a given shale formation, but on the relative abundance of acidity- and alkalinity-generating minerals. The composition of hydraulic fracturing fluid should be tailored according to shale mineralogy. For example, a more acidic fluid could be used with carbonate-rich shales while still permitting high pH conditions in the formation.

3.4.2. Strontium release

Trace metals such as Sr, which is commonly substituted in carbonate minerals (Tesoriero and Pankow, 1996), can be used as tracers of fluid-rock interaction that help identify sources of flowback and produced waters (Capo et al., 2014; Chapman et al., 2012; Phan et al., 2016). Strontium concentrations were tracked over time in the experiments to assess the degree to which mineral dissolution may control Sr concentrations and isotopic compositions in the subsurface. Strontium exhibited an initially rapid release for all shales in the short-term experiments and plateaued at relatively constant values for the majority of the intermediate- and long-term experiments, comparable to the behavior observed for Ca and Mg (Figure 9). The release of Sr is primarily attributed to the dissolution of carbonate minerals, particularly calcite, as has been observed during reaction of the Gothic shale with brine and CO_2, and was inferred to occur during hydraulic fracturing fluid interaction with Marcellus shale at field scale (Jung et al., 2013; Stewart et al., 2015). Similar to the release of U and Pb, the extent of release of Sr under field conditions will therefore depend primarily on the balance between acidity- and alkalinity-generating reactions and the ensuing extent of carbonate mineral dissolution. The rapid dissolution rate of calcite upon contact with the fracturing fluid highlights that the release of Sr from carbonate minerals in the shale formations must be considered when Sr isotopic compositions of produced waters are used to determine the sources and flow paths of these waters. If the Sr isotopic composition of the carbonate in the shale formation is known, the Sr isotopic composition of the fluid can also be used to help constrain the extent of fluid-rock interaction incurred in the fractured formation.

4. Summary and implications for hydraulic fracturing operations

Our experiments revealed that exposure of shales to hydraulic fracturing fluid can induce an array of reactions independent of the exact composition of the shale. The mineralogy of the shale, along with the distribution of the minerals, will strongly dictate the evolution of fluid composition. The simulated fracturing fluid in our experiments prompted extensive dissolution of calcite and pyrite, and minor dissolution of silicate minerals in all shales containing these minerals. The dissolution of calcite tended to generate porosity, which could serve either to enhance hydrocarbon transport, or may lead to weakening of the shale matrix and collapse of fractures. On the other hand, the formation of secondary (oxy)hydroxide phases will clog pore spaces and may block fracture apertures, a process that may contribute to the field-observed inefficient recovery of hydrocarbons. Mineral dissolution reactions released trace metal contaminants to solution that could be brought to the surface with produced and flowback waters, incurring the risk of contaminating surface waters and necessitating treatment of produced waters for safe disposal or re-use (Vengosh et al., 2013, 2014). However, the precipitates were inferred to remove the contaminants from solution via adsorption and/or co-precipitation, which could partially mitigate contaminant transport in the subsurface.

Mineral dissolution-precipitation reactions, rates of aqueous Fe(II) oxidation, and sorption of contaminants are highly sensitive to fluid pH, which was found to be governed most strongly by the mineralogical composition of the rock. Carbonate-rich shales rapidly recovered fluid pH to circum-neutral conditions, whereas fluids in contact with carbonate-poor shales remained acidic. More extensive calcite dissolution generated higher pH, and permitted an apparently greater extent of Fe-(oxy)hydroxide precipitation and more efficient removal of metal contaminants from solution. The implication is that both reaction-induced porosity alteration and the release of contaminants will depend strongly on the volume of fluid injected, as well as the acidity of the fluid and the dissolved oxygen content. Moreover, the mineralogical composition and pore-scale distribution of highly reactive phases, such as pyrite and calcite, will dictate the degree to which contaminants are released and the manner in which porosity develops, as will the effective rock volume with which the fluid reacts (*i.e.*, the degree of imbibition). Further investigation is required to better understand the physical controls on fluid uptake into the matrix and thus the extent of reaction that may occur. In any case, our experiments reveal that both the release of contaminants and formation of porosity-clogging precipitates could be minimized by utilizing fracturing fluids with lower dissolved oxygen content. Although fracturing fluids often include complexing agents designed to inhibit precipitation of secondary phases to minimize mineral scale formation, our experimental results suggest that this practice may counteract the beneficial removal of metal contaminants from solution in the presence of O_2. Overall, our experiments illustrate that fracture fluid compositions and residence times should be adjusted according to shale mineralogy. In carbonate-rich reservoirs, more rapid flushing of fluids, higher acid concentrations, or higher concentrations of Fe-complexing agents would be required compared to carbonate-poor reservoirs to reduce mineral precipitation. In carbonate-poor reservoirs, on the other hand, the low fluid pH may facilitate greater release of metal contaminants (*e.g.*, U, Pb), and therefore more treatment and monitoring of flowback and produced waters may be required. It should also be noted that formation waters typically contain much higher total dissolved solids then were used in our experiments. This difference in initial fluid chemistry may impact some of the reactions observed in our experiments, such as the saturation state of secondary minerals, and the sorption behavior of trace metals. The impacts of high total dissolved solids therefore require further investigation, although the degree to which these fluids may be displaced and diluted, and therefore continue to react within the fractured zone is unknown. Our experiments confirm that a number of reactions can be induced between shales and fluids containing the typical fracturing fluid additives, highlighting the need to better understand these interactions over a variety of geochemical conditions.

Supporting Information

A detailed description of the experimental design, analytical methods, speciation calculation results, and supplementary data are available in the Supporting Information.

Acknowledgments

This research was funded by a National Energy and Technology Laboratory (NETL), Strategic Center for Natural Gas and Oil, grant to SLAC under Department of Energy Contract DE-AC02-76SF00515. ALH was also partially supported by a postdoctoral fellowship from the Natural Sciences and Engineering Research Council of Canada. We appreciate the analytical assistance of Guangchao Li, Doug Turner, Juliet Jamtgaard, Richard Chin, Bob Jones, and Matt Coble. We would like to thank Arjun Kholi for supplying the core samples of both the Eagle Ford and Barnett shales used in this work. A portion of this work was conducted at the Stanford Nano Shared Facilities at Stanford University. This study benefited greatly from discussion with Andrew Kiss, Arjun Kohli, Cindy Ross, Mark Zoback, Yijin Liu, Anthony Kovscek, Mark Hartney, and David Cercone. We thank two anonymous reviewers whose comments greatly improved this manuscript.

References

Al Ismail, M.I., Zoback, M.D., 2016. Effects of rock mineralogy and pore structure on extremely low stress-dependent matrix permeability of unconventional shale gas and shale oil samples. Phil. Trans. R. Soc. A. 374, DOI: 10.1098/rsta.2015.0428.

Ali, M., Hascakir, B., 2015. Water-Rock Interaction for Eagle Ford, Marcellus, Green River, and Barnett. SPE East. Reg. Meet. 1–16.

Andreani, M., Luquot, L., Gouze, P., Godard, M., Hoisé, E., Gibert, B., 2009. Experimental study of carbon sequestration reactions controlled by the percolation of CO_2-rich brine through peridotites. Environ. Sci. Technol. 43, 1226–1231.

Balaba, R.S., Smart, R.B., 2012. Total arsenic and selenium analysis in Marcellus shale, high-salinity water, and hydrofracture flowback wastewater. Chemosphere 89, 1437–1442.

Balashov, V.N., Engelder, T., Gu, X., Fantle, M.S., Brantley, S.L., 2015. A model describing flowback chemistry changes with time after Marcellus Shale hydraulic fracturing. Am. Assoc. Pet. Geol. Bull. 99, 143–154.

Barbot, E., Vidic, N., Gregory, K., Vidic, R., 2013. Spatial and temporal correlation of water quality parameters of produced waters from devonian-age shale follwoing hydraulic fracturing. Environ. Sci. Technol. 47, 2562–2569.

Bargar, J.R., Brown, G.E., Parks, G.A., 1997. Surface complexation of Pb(II) at oxide-water interfaces: II. XAFS and bond-valence determination of mononuclear Pb(II) sorption products and surface functional groups on iron oxides. Geochim. Cosmochim. Acta 61, 2652–2652.

Benjamin, M.M., Leckie, J.O., 1981. Multiple-site adsorption of Cd, Cu, and Pb on amorphous iron oxyhydroxides. J. Colloid Interface Sci. 79, 209–221.

Blauch, M.E., Myers, R.R., Moore, T.R., Lipinski, B.A., Houston, N.A., 2009. Marcellus shale post-frac flowback waters - where is all the salt coming from and what are the implications?, *in*: Society of Petroleum Engineers, Eastern Regional Meeting: Charleston, WV, September 23-25.

Blowes, D.W., Jambor, J.L., Hanton-fong, C.J., Lortie, L., Gould, W.D., 1998. Geochemical , mineralogical and microbiological characterization of a sulphide-bearing carbonate-rich gold-mine tailings impoundment, Joutel, Quebec. Appl. Geochem. 13, 687–705.

Brantley, S.L., Yoxtheimer, D., Arjmand, S., Grieve, P., Vidic, R., Pollak, J., Llewellyn, G.T., Abad, J., Simon, C., 2014. Water resource impacts during unconventional shale gas development: The Pennsylvania experience. Int. J. Coal Geol. 126, 140–156.

Bruno, J., De Pablo, J., Duro, L., Figuerola, E., 1995. Experimental study and modeling of the U(VI)-$Fe(OH)_3$ surface precipitation/coprecipitation equilibria. Geochim. Cosmochim. Acta 59, 4113–4123.

Capo, R.C., Stewart, B.W., Rowan, E.R., Kohl, C.A.K., Wall, A.J., Chapman, E.C., Hammack, R.W., Schroeder, K.T., 2014. The strontium isotopic evolution of Marcellus formation produced waters, southwestern Pennsylvania. Int. J. Coal Geol. 126, 57–63.

Carroll, S.A., McNab, W.W., Dai, Z., Torres, S.C., 2013. Reactivity of Mount Simon Sandstone and the Eau Claire Shale under CO_2 storage conditions. Environ. Sci. Technol. 47, 252–261.

Chalmers, G.R., Bustin, R.M., Power, I.M., 2012. Characterization of gas shale pore systems by porosimetry, pycnometry, surface area, and field emission scanning electron microscopy/transmission electron microscopy image analyses: Examples from the Barnett, Woodford, Haynesville, Marcellus, and Doig units. Am. Assoc. Pet. Geol. Bull. 96, 1099–1119.

Chapman, E.C., Capo, R.C., Stewart, B.W., Kirby, C.S., Hammack, R.W., 2012. Geochemical and strontium isotope characterization of produced waters from Marcellus shale natural gas extraction. Environ. Sci. Technol. 6, 3545–3553.

Chermak, J.A., Schreiber, M.E., 2014. Mineralogy and trace element geochemistry of gas shales in the United States: Environmental implications. Int. J. Coal Geol. 126, 32–44.

Cudennec, Y., Lecerf, A., 2006. The transformation of ferrihydrite into goethite or hematite, revisited. J. Solid State Chem. 179, 716–722.

Duff, M.C., Coughlin, J.U., Hunter, D.B., 2002. Uranium co-precipitation with iron oxide minerals. Geochim. Cosmochim. Acta 66, 3533–3547.

Enid Martinez, C., Mcbride, M.B., 1998. Coprecipitates of Cd, Cu, Pb and Zn in iron oxides: Solid phase transformation and metal solubility after aging and thermal treatment. Clays Clay Miner. 46, 537–545.

FracFocus Chemical Disclosure Registry, 2016. Ground Water Protection Council; Interstate Oil & Gas Compact Commission; https://fracfocus.org

Furrer, G., Phillips, B.L., Ulrich, K.-U., Pöthig, R., Casey, W.H., 2002. The origin of aluminum flocs in polluted streams. Science. 297, 2245–2247.

Golubev, S. V., Benezeth, P., Schott, J., Dandurand, J.L., Castillo, A., 2009. Siderite dissolution kinetics in acidic aqueous solutions from 25 to 100°C and 0 to 50 atm *p*CO_2. Chem. Geol. 260, 295–301.

Gouze, P., Luquot, L., 2011. X-ray microtomography characterization of porosity, permeability and reactive surface changes during dissolution. J. Contam. Hydrol. 120–121, 45–55.

Haluszczak, L.O., Rose, A.W., Kump, L.R., 2013. Geochemical evaluation of flowback brine from Marcellus gas wells in Pennsylvania, USA. Appl. Geochem. 28, 55–61.

Hammack, R.W., Harbert, W., Sharma, S., Stewart, B.W., Capo, R.C., Wall, A.J., Wells, A., Diehl, R., Blaushild, D., Sams, J., Veloski, G., 2014. An evaluation of fracture growth and gas/fluid migration as horizontal Marcellus Shale gas wells are hydraulically fractured in Greene County, Pennsylvania. National Energy Technology Laboratory: Pittsburgh, 2014; p 76.

Harrison, A.L., Dipple, G.M., Power, I.M., Mayer, K.U., 2016. The impact of evolving mineral-water-gas interfacial areas on mineral-fluid reaction rates in unsaturated porous media. Chem. Geol. 421, 65–80.

Harrison, A.L., Dipple, G.M., Power, I.M., Ulrich Mayer, K., 2015. Influence of surface passivation and water content on mineral reactions in unsaturated porous media: Implications for brucite carbonation and CO_2 sequestration. Geochim. Cosmochim. Acta 148, 477–495.

Jambor, J.L., Dutrizac, J.E., 1998. Occurrence and constitution of natural and synthetic ferrihydrite, a widespread iron oxyhydroxide. Chem. Rev. 98, 2549–2586.

Jennings, D.S., Antia, J., 2013. Petrographic characterization of the Eagle Ford shale, South Texas: Mineralogy, common constituents, and distribution of nanometer-scale pore types. *in*: W. Camp, E. Diaz, and B. Wawak, eds., Electron microscopy of shale hydrocarbon reservoirs: AAPG Memoir 102, p. 101–113.

Jew, A.D., Dustin, M.K., Harrison, A.L., Joe-Wong, C.M., Thomas, D.L., Maher, K.M., Brown, G.E. Jr., Bargar, J.R., *in review*. Impact of organics and carbonates on the oxidation and precipitation of iron during hydraulic fracturing of shale. Energy & Fuels.

Jin, L., Mathur, R., Rother, G., Cole, D., Bazilevskaya, E., Williams, J., Carone, A., Brantley, S., 2013. Evolution of porosity and geochemistry in Marcellus Formation black shale during weathering. Chem. Geol. 356, 50–63.

Johnston, J.H., Lewis, D.G., 1983. A detailed study of the transformation of ferrihydrite to hematite in an aqueous medium at 92°C. Geochim. Cosmochim. Acta 47, 1823–1831.

Jung, H.B., Um, W., Cantrell, K.J., 2013. Effect of oxygen co-injected with carbon dioxide on Gothic shale caprock-CO_2-brine interaction during geologic carbon sequestration. Chem. Geol. 354, 1–14.

Kerr, R.A., 2010. Natural gas from shale bursts onto the scence. Science. 328, 1624–1626.

Law, B.E., Pollastro, R.M., Keighin, C.W., 1986. Geologic characterization of low-permeability gas reservoirs in selected wells, greater Green River Basin, Wyoming, Colorado, and Utah, *in*: AAPG Special Volumes: SG 24: Geology of Tight Gas Reservoirs. pp. 253–169.

Lester, Y., Ferrer, I., Thurman, E.M., Sitterley, K.A., Korak, J.A., Aiken, G., Linden, K.G., 2015. Characterization of hydraulic fracturing flowback water in Colorado:

Implications for water treatment. Sci. Total Environ. 512–513, 637–644.

Luquot, L., Andreani, M., Gouze, P., Camps, P., 2012. CO_2 percolation experiment through chlorite/zeolite-rich sandstone (Pretty Hill Formation – Otway Basin–Australia). Chem. Geol. 294–295, 75–88.

Luquot, L., Gouze, P., 2009. Experimental determination of porosity and permeability changes induced by injection of CO_2 into carbonate rocks. Chem. Geol. 265, 148–159.

Materials Data, Inc., 2002. Jade XRD Pattern Processing Ver. 6.5.

Michel, F.M., Barrón, V., Torrent, J., Morales, M.P., Serna, C.J., Boily, J.-F., Liu, Q., Ambrosini, A., Cismasu, a C., Brown, G.E., 2010. Ordered ferrimagnetic form of ferrihydrite reveals links among structure, composition, and magnetism. Proc. Natl. Acad. Sci. U.S.A. 107, 2787–2792.

Morel, F. M. M., J. G. Hering, 1993. Principles and applications of aquatic chemistry. Wiley-Interscience, New York, 588 pp

Morgan, B., Lahav, O., 2007. The effect of pH on the kinetics of spontaneous Fe(II) oxidation by O_2 in aqueous solution - basic principles and a simple heuristic description. Chemosphere 68, 2080–2084.

Nicholson, R. V., Gillham, R.W., Reardon, E.J., 1990. Pyrite oxidation in carbonate-buffered solution: 2. Rate control by oxide coatings. Geochim. Cosmochim. Acta 54, 395–402.

Nordstrom, D. K., 1982. Aqueous pyrite oxidation and the consequent formation of secondary iron minerals. Acid sulfate weathering, 37-56.

Orem, W., Tatu, C., Varonka, M., Lerch, H., Bates, A., Engle, M., Crosby, L., McIntosh, J., 2014. Organic substances in produced and formation water from unconventional natural gas extraction in coal and shale. Int. J. Coal Geol. 126, 20–31.

Palandri J. L. and Kharaka Y. K. (2004) A compilation of rate parameters of water–mineral interaction kinetics for application to geochemical modeling. US Geol. Sur. Open File Rep. 2004-1068.

Parkhurst, D.L., Appelo, C.A.J., 2013. Description of input and examples for PHREEQC Version 3 — A computer program for speciation , batch-reaction , one-dimensional transport, and inverse geochemical calculations, in: U.S. Geological Survey Techniques and Methods, Book 6, Chap. A43, 497 P. Denver, Colorado, p. 497.

Phan, T.T., Capo, R.C., Stewart, B.W., Graney, J.R., Johnson, J.D., Sharma, S., Toro, J., 2015. Trace metal distribution and mobility in drill cuttings and produced waters from Marcellus Shale gas extraction: Uranium, arsenic, barium. Appl. Geochem. 60, 89–103.

Phan, T.T., Capo, R.C., Stewart, B.W., Macpherson, G.L., Rowan, E.L., Hammack, R.W., 2016. Factors controlling Li concentration and isotopic composition in formation waters and host rocks of Marcellus Shale, Appalachian Basin. Chem. Geol. 420, 162–179.

Pokrovsky, O.S., Golubev, S. V., Schott, J., 2005. Dissolution kinetics of calcite, dolomite and magnesite at 25 °C and 0 to 50 atm pCO_2. Chem. Geol. 217, 239–255.

Renock, D., Landis, J.D., Sharma, M., 2016. Reductive weathering of black shale and release of barium during hydraulic fracturing. Appl. Geochem. 65, 73–86.

Rimstidt, D.D., Vaughan, D.J., 2003. Pyrite oxidation: A state-of-the-art assessment of the reaction mechanism. Geochim. Cosmochim. Acta 67, 873–880.

Rowan, E.L., Engle, M.A., Kraemer, T.F., Schroeder, K.T., Hammack, R.W., Doughten, M.W., 2015. Geochemical and isotopic evolution of water produced from Middle Devonian Marcellus shale gas wells, Appalachian basin, Pennsylvania. Am. Assoc. Pet. Geol. Bull. 99, 181–206.

Roychaudhuri, B., Tsotsis, T.T., Jessen, K., 2013. An experimental investigation of spontaneous imbibition in gas shales. J. Pet. Sci. Eng. 111, 87–97.

Schwertmann, U., Friedl, J., Stanjek, H., 1999. From Fe(III) ions to ferrihydrite and then to hematite. J. Colloid Interface Sci. 209, 215–223.

Shih, J.-S., Saiers, J.E., Anisfeld, S.C., Chu, Z., Muehlenbachs, L.A., Olmstead, S.M., 2015. Characterization and analysis of liquid waste from Marcellus shale gas development. Environ. Sci. Technol. 49, 9557–9565.

Smith, M.M., Wolery, T.J., Carroll, S.A., 2013. Kinetics of chlorite dissolution at elevated temperatures and CO_2 conditions. Chem. Geol. 347, 1–8.

Steefel, C.I., Van Cappellen, P., 1990. A new kinetic approach to modeling water-rock interaction: The role of nucleation, precursors, and Ostwald ripening. Geochim. Cosmochim. Acta 54, 2657–2677.

Stewart, B.W., Chapman, E.C., Capo, R.C., Johnson, J.D., Graney, J.R., Kirby, C.S., Schroeder, K.T., 2015. Origin of brines, salts and carbonate from shales of the Marcellus Formation: Evidence from geochemical and Sr isotope study of sequentially extracted fluids. Appl. Geochem. 60, 78–88.

Stringfellow, W.T., Domen, J.K., Camarillo, M.K., Sandelin, W.L., Borglin, S., 2014. Physical, chemical, and biological characteristics of compounds used in hydraulic fracturing. J. Hazard. Mater. 275, 37–54.

Stumm, W., Lee, G.F., 1961. Oxygenation of ferrous iron. Ind. Eng. Chem. 53, 143–146.

Tesoriero, A.J., Pankow, J.F., 1996. Solid solution partitioning of Sr^{2+}, Ba^{2+}, and Cd^{2+} to calcite. Science. 60, 1053–1063.

Tuttle, M.L.W., Breit, G.N., Goldhaber, M.B., 2009. Weathering of the New Albany Shale, Kentucky: II. Redistribution of minor and trace elements. Appl. Geochem. 24, 1565–1578.

U.S Energy Information Administration, 2013. Technically recoverable shale oil and shale gas resources: An assessment of 137 shale formations in 41 countries outside the Unites States. EIA report: Washington, D.C., 2013; p 76. http://www.eia.gov/analysis/studies/worldshalegas/pdf/overview.pdf

Vengosh, A., Jackson, R.B., Warner, N., Darrah, T.H., Kondash, A., 2014. A critical review of the risks to water resources from shale gas development and hydraulic fracturing in the United States. Environ. Sci. Technol. 16, 8334–8348.

Vengosh, A., Warner, N., Jackson, R., Darrah, T., 2013. The effects of shale gas exploration and hydraulic fracturing on the quality of water resources in the United States. Procedia Earth Planet. Sci. 7, 863–866.

Vidic, R.D., Brantley, S.L., Vandenbossche, J.M., Yoxtheimer, D., Abad, J.D., 2013. Impact of shale gas development on regional water quality. Science. 340, 1235009-1–1235009-9.

Wang, L., Fortner, J.D., Giammar, D.E., 2015. Impact of water chemistry on element mobilization from Eagle Ford shale. Environ. Eng. Sci. 32, 310–320.

Ziemkiewicz, P.F., Thomas He, Y., 2015. Evolution of water chemistry during Marcellus shale gas development: A case study in West Virginia. Chemosphere 134, 224–231.

Zolfaghari, A., Dehghanpour, H., Noel, M., Bearinger, D., 2016. Laboratory and field analysis of flowback water from gas shales. J. Unconv. Oil Gas Resour. 14, 113–127.

Table 1. Initial chemical composition of shale samples[a]

Element[b]	Barnett	Marcellus	Green River	Eagle Ford
Na (wt.%)	0.10	< 0.01	0.94	< 0.01
Mg (wt.%)	0.63	0.78	4.41	0.37
Al (wt.%)	7.29	10.50	2.66	5.82
Si (wt.%)	25.53	28.41	12.27	15.97
S (wt.%)	0.90	2.05	0.10	1.13
K (wt.%)	1.65	2.07	1.07	0.89
Ca (wt.%)	2.51	4.23	13.64	16.67
Fe (wt.%)	2.48	4.56	1.78	2.12
Ni (μg/g)	126.4	275.1	27.1	71.2
U (μg/g)	2.6	33.5	3.8	< 0.4
Pb (μg/g)	12.9	32.5	16.4	11.5
Sr (μg/g)	275.3	182.6	884.1	494.7
Mn (μg/g)	172.9	209.2	290.8	90.0
As (μg/g)	10.3	32.4	11.9	19.7

[a] Data are from x-ray fluorescence analysis and are reproduced from Jew et al. (*in press*).
[b] Uncertainty for triplicate measurements is ≤ 5%.

Table 2. Initial mineralogical composition of shale samples based on x-ray diffraction analysis[a]

	Carbonate-poor		Carbonate-rich	
Mineral (wt.%)[b]	Barnett	Marcellus	Green River	Eagle Ford
Quartz	44.2	42.2	31.4	25.2
Feldspars	4.9	3.7	8.0	nd[c]
Calcite	8.2	11.6	23.2	64.5
Dolomite	nd	1.1	28.9	nd
Pyrite	2.1	6.4	nd	2.7
Analcime	nd	nd	8.5	nd
Clays	40.6	35	nd	7.6

[a] Data reproduced from Jew et al. (*in press*).
[b] analytical uncertainty is ≤ 15 wt.%
[c] nd = not detected

Figure Captions

Figure 1. Aqueous concentrations of (a) calcium, (b) pH, (c) iron, and (d) sulfate versus reaction time for all short-term experiments. Inset in (a) shows the percentage of total Ca remaining in the solid phase based on x-ray fluorescence spectroscopy of the initial solids and final aqueous Ca concentrations. The labels B, B2, M, EF, and GR represent the short-term Barnett, Barnett duplicate, Marcellus, Eagle Ford, and Green River experiments, respectively. Dashed lines in (c) represent calculated Fe concentrations based on measured SO_4^{2-} concentrations, assuming stoichiometric pyrite dissolution. Duplicate reactors are distinguished by filled versus unfilled symbols of the same type. Analytical error is smaller than symbol size unless otherwise shown.

Figure 2. Aqueous concentrations of (a) calcium, (b) pH, (c) iron, and (d) sulfate versus reaction time in all intermediate- and long-term experiments. Dashed and solid lines without symbols in (c) represent calculated Fe concentrations based on measured SO_4^{2-} concentrations, assuming stoichiometric pyrite dissolution. Line colors correspond to color coding for shale type as indicated in (a). Duplicate reactors are distinguished by filled versus unfilled symbols of the same type or different dash types for dashed lines. Analytical error is smaller than symbol size unless otherwise shown.

Figure 3. Silicon (a) and aluminum (b) concentrations versus reaction time in short-term experiments. Duplicate reactors are distinguished by filled versus unfilled symbols of the same type. Analytical error is smaller than symbol size unless otherwise shown. Silicon

and aluminum mass balance (c) displayed as the percentage of total Si or Al remaining in the solid phase based on x-ray fluorescence spectroscopy of the initial solids and final aqueous Si and Al concentrations. Solid and striped bars represent Si and Al, respectively.

Figure 4. Saturation indices of secondary Fe(III)-bearing phases versus reaction time in the Marcellus (a) and Barnett (b) experiments of all durations. For clarity, only one of the Marcellus duplicates for the intermediate- and long-term experiments is shown. Orange, red, and black lines represent goethite [α-FeO(OH)], hematite [α-Fe_2O_3], and amorphous $Fe(OH)_3$, respectively. The solid grey line indicates chemical equilibrium with respect to a given solid phase (*i.e.* saturation index = 0).

Figure 5. Saturation index of calcite [$CaCO_3$] in all experiments. Data from the short-, intermediate-, and long-term experiments are represented by triangles, circles, and squares, respectively. Duplicate reactors are distinguished by filled versus unfilled symbols of the same type. The black dashed line indicates chemical equilibrium with respect to calcite (*i.e.* saturation index = 0).

Figure 6. Scanning electron micrographs of reacted versus unreacted shale samples. Barnett unreacted (a), Barnett reacted (b), Marcellus unreacted (c), Marcellus reacted (d), Green River unreacted (e), Green River reacted (f), Eagle Ford unreacted (g), and Eagle Ford reacted (h).

Figure 7. Aqueous Ni concentration versus time for the Barnett, Eagle Ford (EF), and Green River (GR) reactors of all durations (a). Aqueous Ni (b), Pb (c), and U (d) concentration versus time for Marcellus reactors of all durations. Duplicate reactors are distinguished by filled versus unfilled symbols of the same type. Analytical error is smaller than symbol size unless otherwise shown.

Figure 8. Maximum measured aqueous Pb, U, and Ni concentrations versus maximum measured pH in Marcellus reactors of all durations (a). Analytical error is smaller than symbol size unless otherwise shown. Aqueous Fe to S molar ratios versus pH for all time points in Marcellus reactors of all durations (b). Duplicate reactors are distinguished by filled versus unfilled symbols of the same type.

Figure 9. Aqueous Sr concentration versus time in all reactors. Duplicate reactors are distinguished by filled versus unfilled symbols of the same type. Analytical error is smaller than symbol size unless otherwise shown.

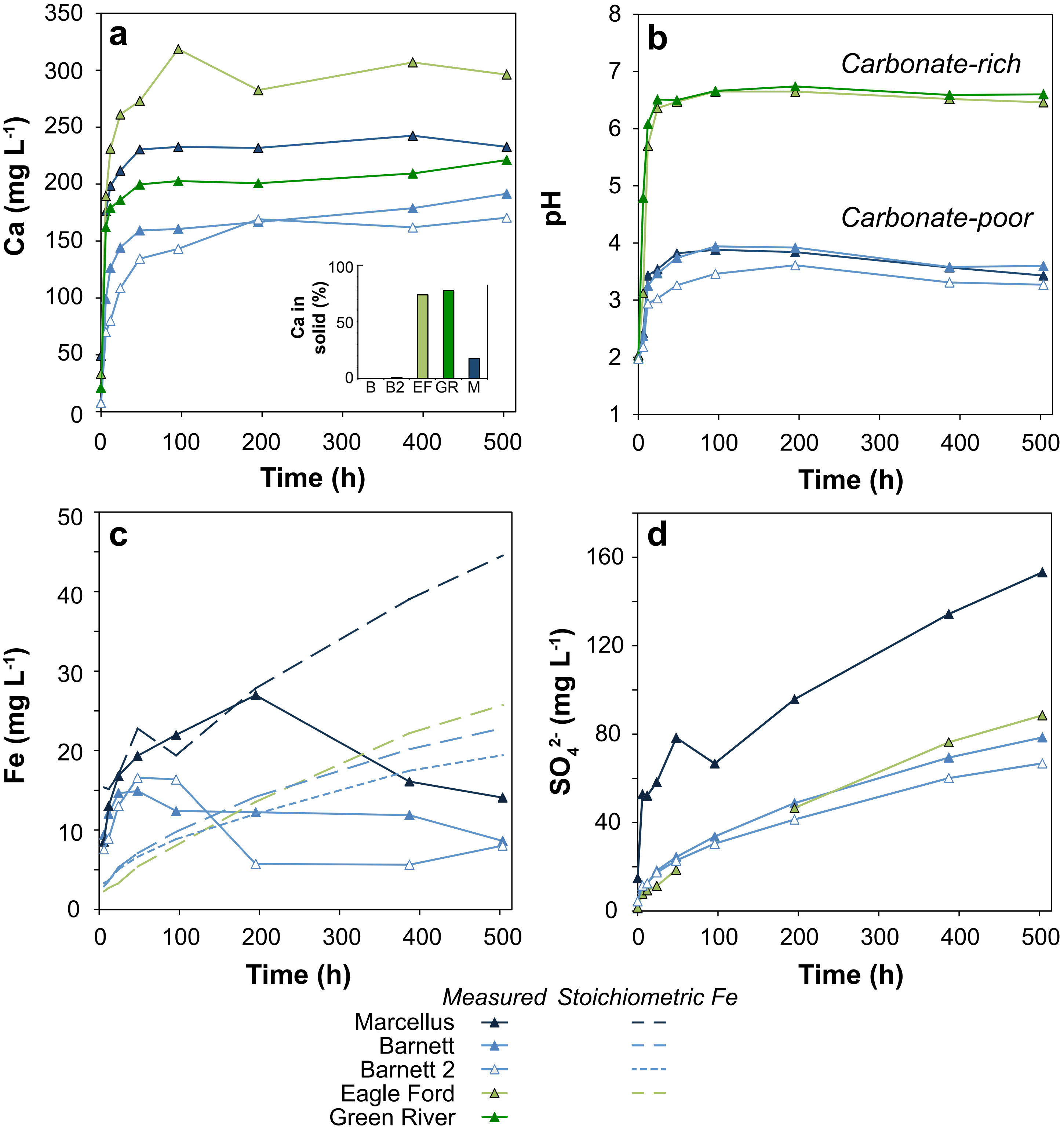
a
Ca (mg L-1)
350
300
250
200
150
100
50
0
Time (h)
0
100
200
300
400
500
Ca in solid (%)
100
50
0
B
B2
EF
GR
M
b
pH
8
7
6
5
4
3
2
1
Carbonate-rich
Carbonate-poor
Time (h)
c
Fe (mg L-1)
50
40
30
20
10
0
Time (h)
d
SO4 2- (mg L-1)
160
120
80
40
0
Time (h)
Measured
Stoichiometric Fe
Marcellus
Barnett
Barnett 2
Eagle Ford
Green River

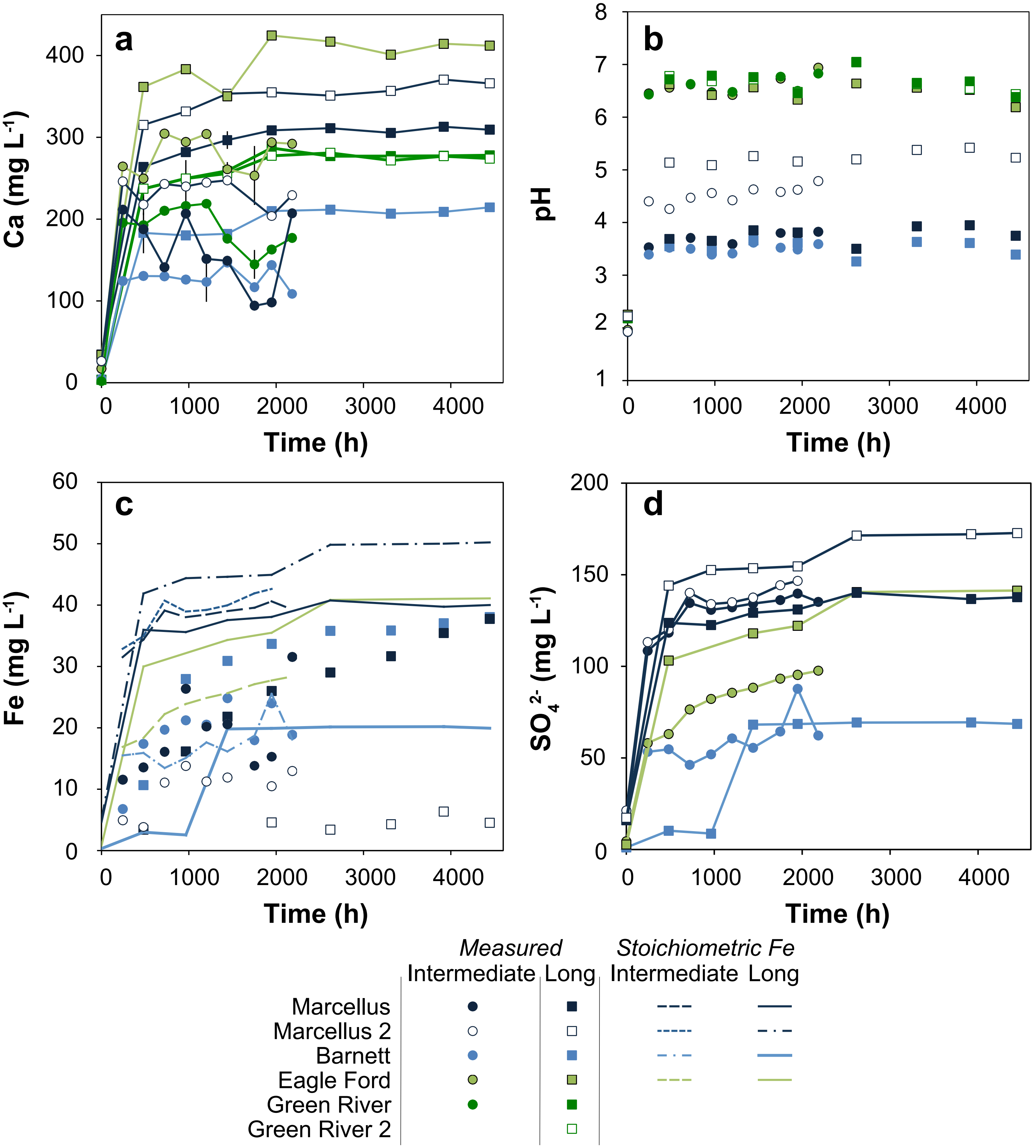
a
Ca (mg L^{-1})
0
100
200
300
400
0
1000
2000
3000
4000
Time (h)
b
pH
1
2
3
4
5
6
7
8
0
1000
2000
3000
4000
Time (h)
c
Fe (mg L^{-1})
0
10
20
30
40
50
60
0
1000
2000
3000
4000
Time (h)
d
SO$_4^{2-}$ (mg L^{-1})
0
50
100
150
200
0
1000
2000
3000
4000
Time (h)
Measured
Intermediate
Long
Stoichiometric Fe
Intermediate
Long
Marcellus
Marcellus 2
Barnett
Eagle Ford
Green River
Green River 2

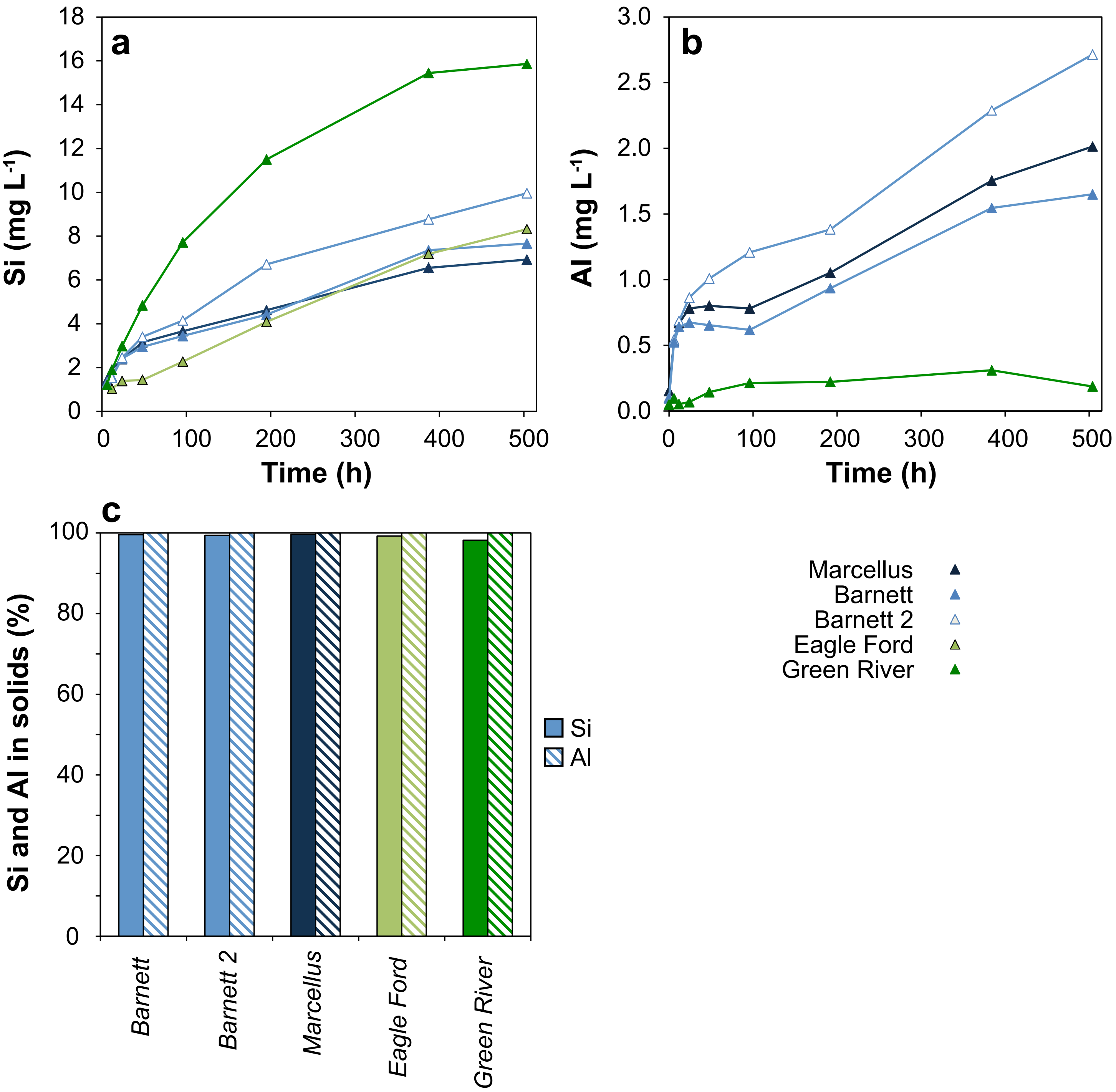
a
Si (mg L-1)
0
2
4
6
8
10
12
14
16
18
0
100
200
300
400
500
Time (h)
b
Al (mg L-1)
0.0
0.5
1.0
1.5
2.0
2.5
3.0
0
100
200
300
400
500
Time (h)
c
Si and Al in solids (%)
0
20
40
60
80
100
Barnett
Barnett 2
Marcellus
Eagle Ford
Green River
Si
Al
Marcellus
Barnett
Barnett 2
Eagle Ford
Green River

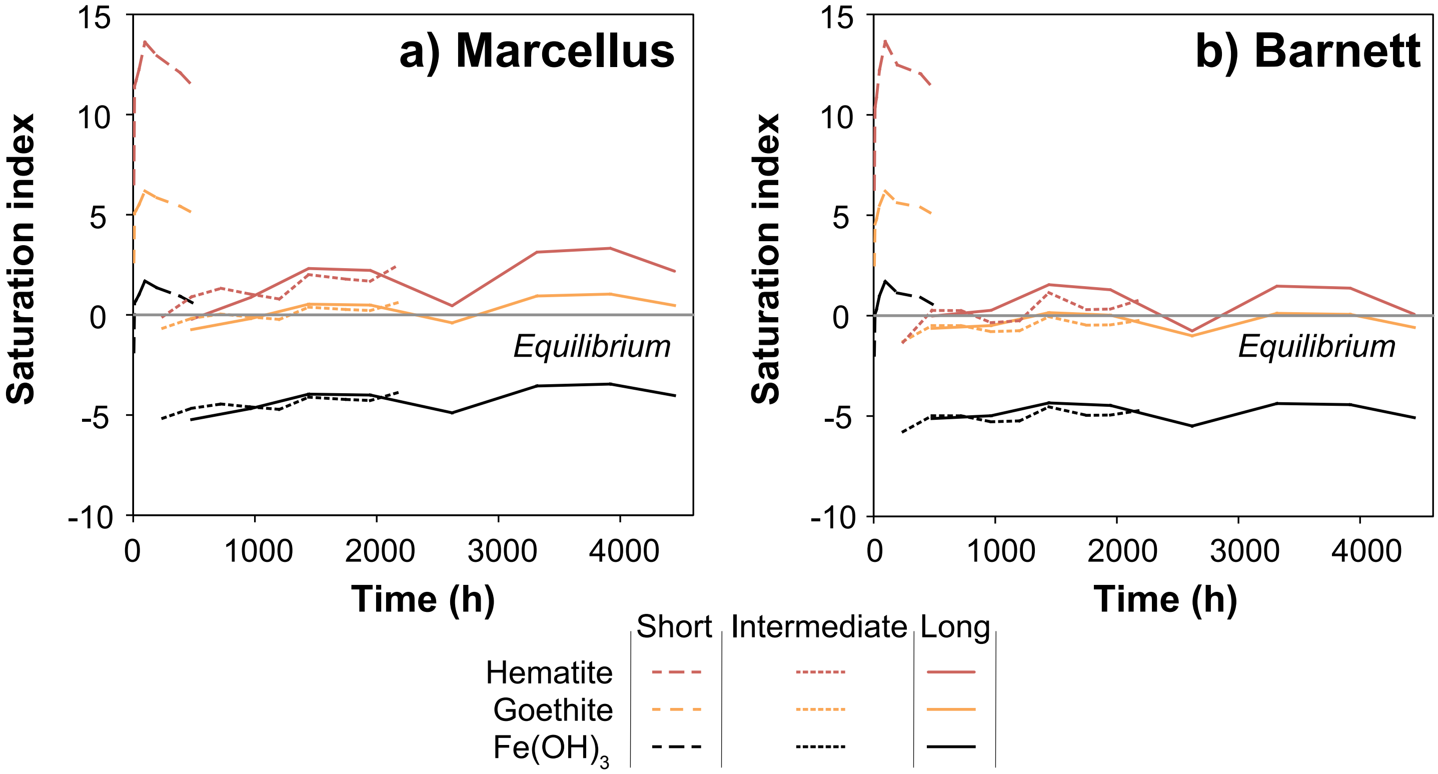
a) Marcellus
b) Barnett
Saturation index
15
10
5
0
-5
-10
Time (h)
0
1000
2000
3000
4000
Equilibrium
Short
Intermediate
Long
Hematite
Goethite
Fe(OH)3

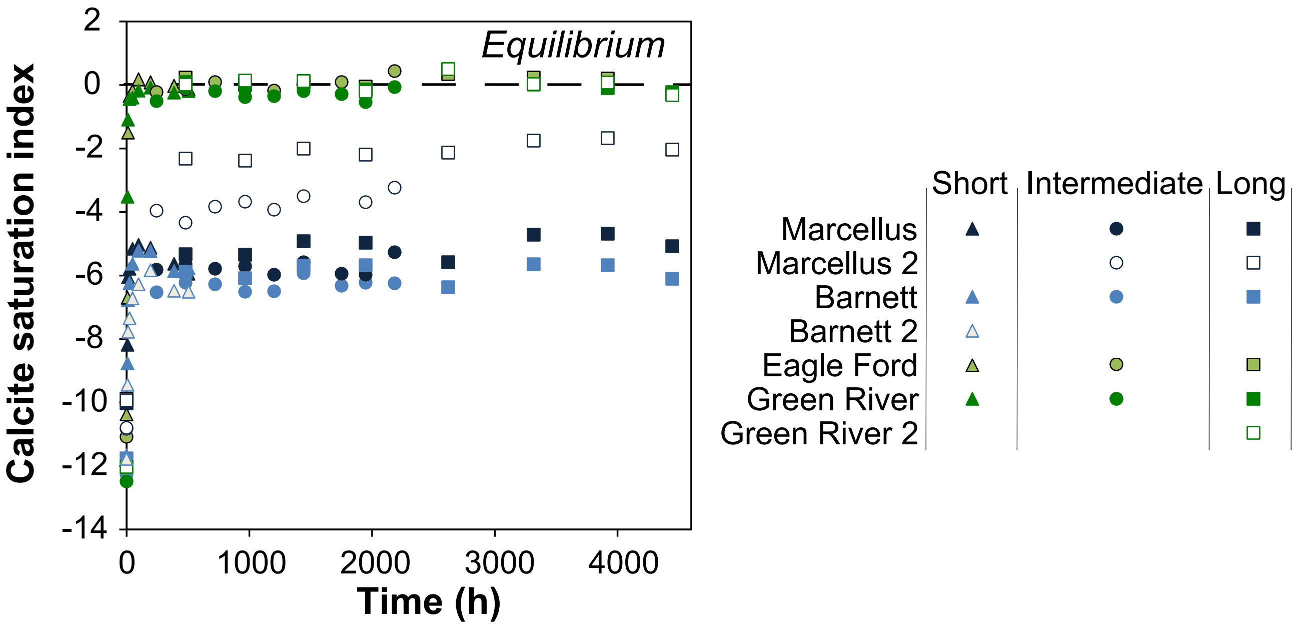
Equilibrium
Calcite saturation index
2
0
-2
-4
-6
-8
-10
-12
-14
0
1000
2000
3000
4000
Time (h)
Short
Intermediate
Long
Marcellus
Marcellus 2
Barnett
Barnett 2
Eagle Ford
Green River
Green River 2

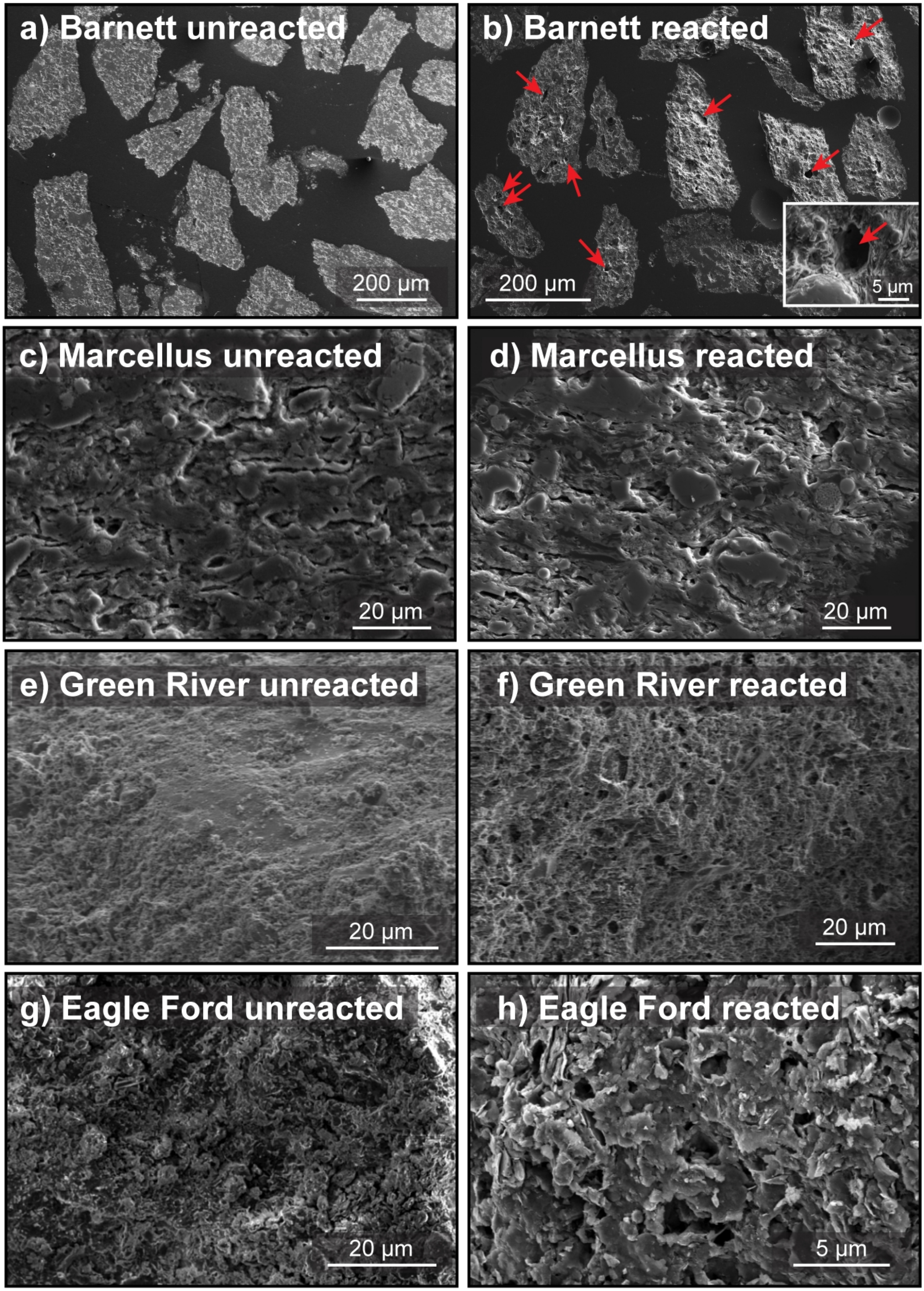
a) Barnett unreacted
200 μm
b) Barnett reacted
200 μm
5 μm
c) Marcellus unreacted
20 μm
d) Marcellus reacted
20 μm
e) Green River unreacted
20 μm
f) Green River reacted
20 μm
g) Eagle Ford unreacted
20 μm
h) Eagle Ford reacted
5 μm

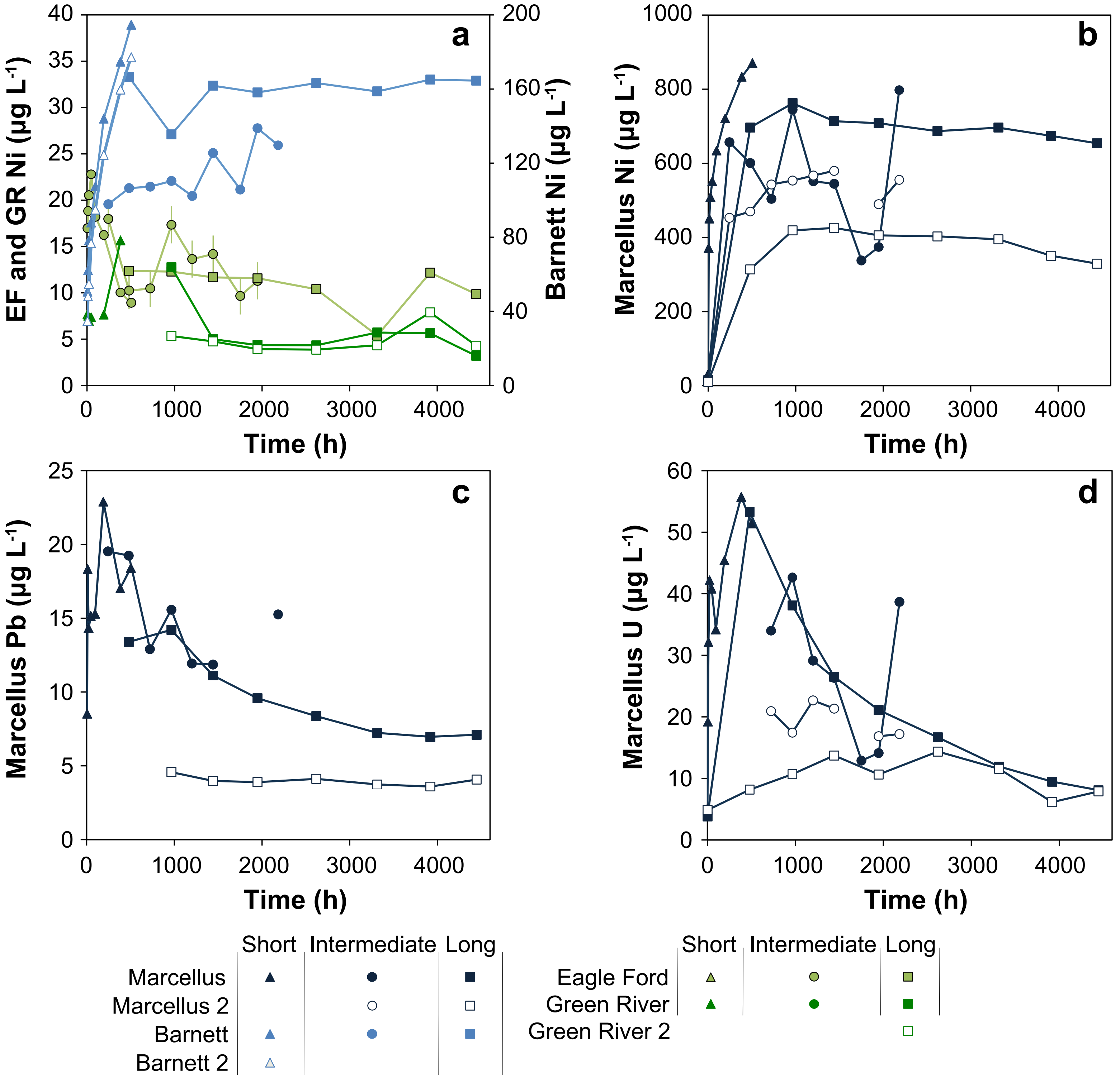
a
EF and GR Ni (µg L-1)
Barnett Ni (µg L-1)
0
5
10
15
20
25
30
35
40
0
40
80
120
160
200
Time (h)
0
1000
2000
3000
4000
b
Marcellus Ni (µg L-1)
0
200
400
600
800
1000
Time (h)
c
Marcellus Pb (µg L-1)
0
5
10
15
20
25
Time (h)
d
Marcellus U (µg L-1)
0
10
20
30
40
50
60
Time (h)
Short
Intermediate
Long
Marcellus
Marcellus 2
Barnett
Barnett 2
Eagle Ford
Green River
Green River 2

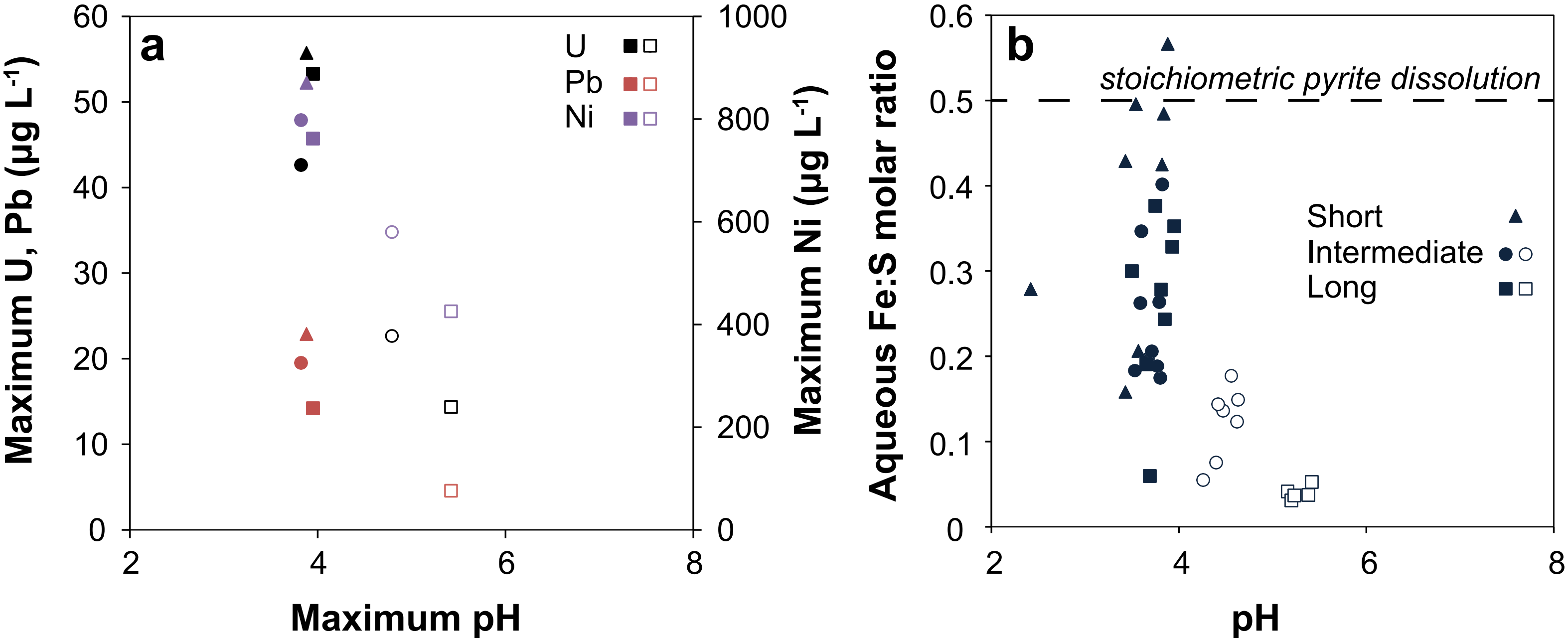
a
Maximum U, Pb (μg L-1)
0
10
20
30
40
50
60
Maximum Ni (μg L-1)
0
200
400
600
800
1000
Maximum pH
2
4
6
8
U ■ □
Pb ■ □
Ni ■ □
b
Aqueous Fe:S molar ratio
0
0.1
0.2
0.3
0.4
0.5
0.6
pH
2
4
6
8
stoichiometric pyrite dissolution
Short ▲
Intermediate ● ○
Long ■ □

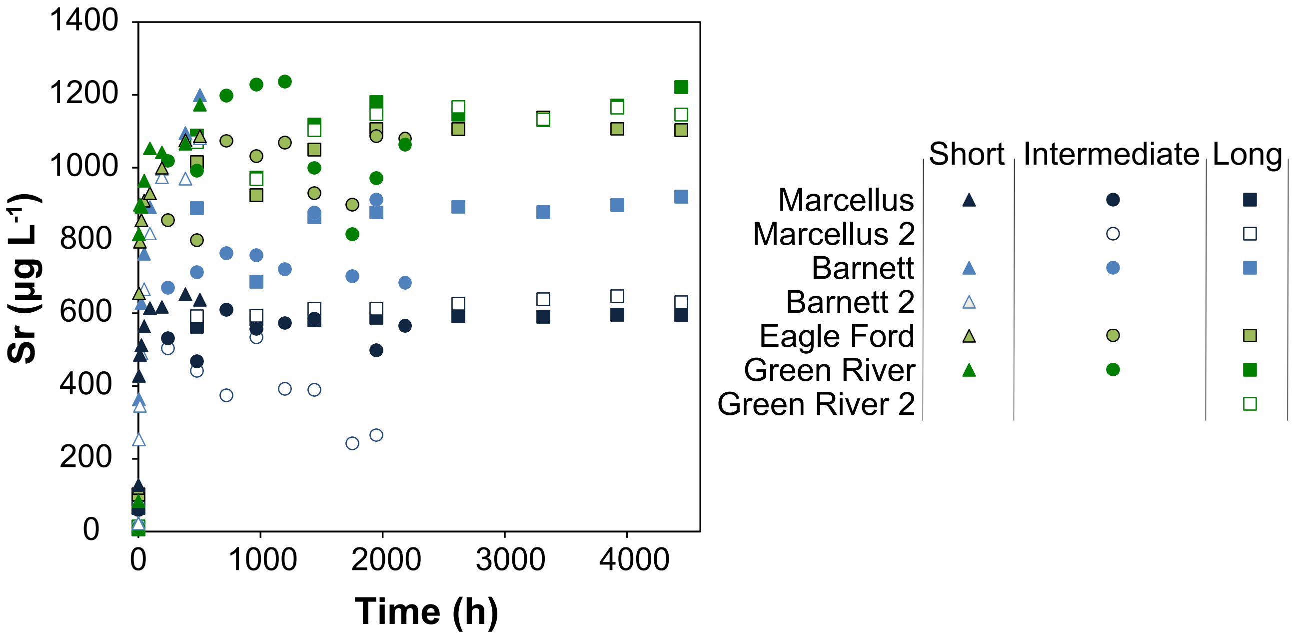
Sr (µg L-1)
0
200
400
600
800
1000
1200
1400
Time (h)
0
1000
2000
3000
4000
Short
Intermediate
Long
Marcellus
Marcellus 2
Barnett
Barnett 2
Eagle Ford
Green River
Green River 2